

# A novel DNAJ protein, TCAIM, drives proteolysis of $\alpha$ -ketoglutarate dehydrogenase and regulates mitochondrial metabolism.

**Jiahui WANG**

School of Medicine, Shanghai Jiaotong University

**Youhuang ZHONG**

School of Medicine, Shanghai Jiaotong University

**Xiaomin Ma**

Southern University of Science and Technology

**Yuanzhu Gao**

Sun Yat-sen University

**Dejian ZHOU**

State Key Laboratory of Genetic Engineering, School of Life Sciences, Fudan University,

**Jie Wang**

Department of Biochemistry and Molecular & Cell Biology, School of Medicine, Shanghai Jiao Tong University

**Yinkun Fu**

Shanghai Jiaotong University School of Medicine

**Yutong HOU**

School of Medicine, Shanghai Jiaotong University

**Fan SHI**

School of Medicine, Shanghai Jiaotong University

**Yu Zhang**

Department of Biochemistry and Molecular & Cell Biology, School of Medicine, Shanghai Jiao Tong University

**Yingjie Xu**

School of Medicine, Shanghai Jiao Tong University, Shanghai, P.R. China <https://orcid.org/0000-0002-8461-6974>

**peiyi wang**

Southern University of Science & Technology

**Marcia Haigis**

Harvard Medical School <https://orcid.org/0000-0003-2530-2681>

**Xiang Yu**

Department of Biochemistry and Molecular & Cell Biology, School of Medicine, Shanghai Jiao Tong University

Wen Yang (✉ [yangwen@shsmu.edu.cn](mailto:yangwen@shsmu.edu.cn))

School of Medicine, Shanghai Jiaotong University <https://orcid.org/0000-0002-2032-1982>

---

## Article

**Keywords:** TCAIM, Mitochondria,  $\alpha$ -ketoglutarate dehydrogenase, OGDH, proteostasis, DNAJC, single-particle cryo-EM

**Posted Date:** January 21st, 2022

**DOI:** <https://doi.org/10.21203/rs.3.rs-1236697/v1>

**License:**   This work is licensed under a Creative Commons Attribution 4.0 International License.

[Read Full License](#)

---

# Abstract

Mitochondria play essential roles in metabolism, and the proteostasis system is important for almost all biological processes that occur in this double-membrane-enclosed organelle, including metabolic functions. In this study, we identified a novel mtHSP70 co-chaperone DNAJC protein, TCAIM, that specifically binds to the E1 subunit of  $\alpha$ -ketoglutarate dehydrogenase (OGDH). Using the single-particle cryo-EM technique, we determined the binding structures of TCAIM and OGDH. We further demonstrated that by binding to the native form of OGDH, TCAIM specifically mediates the degradation of OGDH and regulates its activity *in vivo* in a mtHSP70- and LONP1-dependent manner. Moreover, the lack of TCAIM changes metabolism in mice and primary cells, whereas overexpression of TCAIM decreases mitochondrial bioenergetics. Thus, this study revealed a novel mechanism by which mitochondrial metabolism could be regulated by selective degradation of an important metabolic enzyme, mediated by a DNAJC protein.

## Introduction

Mitochondria are the central organelles for bioenergetics and are crucial for many metabolic pathways, including biosynthesis and catabolism of glucose, fatty acids, and amino acids. The tricarboxylic acid (TCA) cycle not only generates nicotinamide adenine dinucleotide (NADH) and reduced flavine adenine dinucleotide (FADH<sub>2</sub>) for ATP production, but also provides intermediates for various metabolic processes. Some TCA cycle enzymes are large protein complexes, such as the  $\alpha$ -ketoglutarate dehydrogenase complex (OGDHC), located in the mitochondrial matrix. The function of these macromolecules needs to be maintained and regulated in a timely manner to coordinate with biochemical processes occurring inside and outside the mitochondria<sup>1</sup>. OGDHC consists of three different subunits: the E1 subunit, 2-oxoglutarate dehydrogenase (OGDH); the E2 subunit, dihydrolipoyllysine succinyltransferase (DLST); and the E3 subunit, D-2-hydroxyglutarate pyruvate transhydrogenase (DLD). This enzyme catalyzes the reaction between  $\alpha$ -ketoglutarate and CoA to reduce NAD<sup>+</sup> to NADH and generate succinyl-CoA and CO<sub>2</sub><sup>2</sup>. OGDHC is a rate-limiting enzyme of the tricarboxylic acid (TCA) cycle and plays a unique role in various metabolic pathways. Its substrate,  $\alpha$ -ketoglutarate, is located at the crossroads of the TCA cycle and glutamine catabolism. Therefore, regulation of its function has been of interest for decades. OGDHC activity is regulated by the NAD<sup>+</sup>/NADH ratio, ADP/ATP ratio, and Pi concentration<sup>3</sup>. However, little is known about how these subunits and the stoichiometry of the protein complex are regulated post-translationally.

One of the most important mechanisms of post-translational regulation is protein degradation, an important part of protein homeostasis, or “proteostasis.” In the mitochondria, proteostasis is essential for maintaining its metabolic functions, and its malfunction is a cause of many metabolic disorders related to ageing<sup>4</sup>. In the mitochondrial matrix, proteostasis systems include heat shock proteins, such as hsp70 (HSPA9) and hsp40 co-chaperones (also called DNAJ proteins for their common DNAJ domain), which

fold and unfold proteins. They also include proteases, such as LONP1, CLPXP, and AFG3L2, to degrade misfolded or damaged proteins<sup>1,5</sup>.

A general notion for proteostasis is that intrinsically unstructured proteins need to be stabilized to prevent degradation by default, while the degradation of stabilized proteins in case of specific regulation relies on polyubiquitination to be recognized by proteasomes for degradation<sup>6</sup>. Little is known about how mitochondrial matrix proteins are specifically targeted by proteases for degradation and whether proteostasis can selectively impact certain metabolic pathways. Several recent studies have established that mitochondrial matrix proteins can be polyubiquitinated or oxidized, followed by targeted degradation<sup>7-9</sup>. These findings raise the possibility that mitochondrial protein degradation could assist in metabolic regulation by specifically targeting essential metabolic enzymes.

In this study, through proteomic analysis, we identified a novel DNAJ protein, TCAIM, which specifically binds to and regulates OGDH. Further studies indicated that TCAIM profoundly affects mitochondrial metabolism. Moreover, enzymatic assays and structural biology approaches have confirmed that TCAIM binds to the native form of OGDH and mediates its protein degradation.

## Results

### OGDH interacts with TCAIM, a mitochondrial DNAJ protein

Our previous proteomics study identified TCAIM (encoded by *TCAIM*, also known as *C3orf23*) as a specific interacting protein of OGDH, through immunoprecipitation coupled with mass spectrometry (IP-MS) of HA-tagged OGDH (OGDH-HA)<sup>10</sup>. This interaction was further confirmed by reverse IP-MS and IP-western blotting, using TCAIM-HA as bait (Fig. 1A&B, Fig S1A and Table S1). TCAIM contains a highly conserved N-terminal DNAJ domain (J domain) and the HPD motif but lacks glycine-rich segments attached to its J domain, indicating that TCAIM belongs to the type III DNAJ/HSP40 family (Fig. 1C&D and Fig S1B-D)<sup>11</sup>. DNAJ proteins are well-known co-chaperones of HSP70. Indeed, mitochondrial HSP70 (HSPA9) was among the most abundant interacting proteins of TCAIM (Fig S1A and Table S1).

TCAIM also contains a single C-terminal domain of unknown function; we suspect that this domain is responsible for its binding with OGDH. To verify the interaction between OGDH and TCAIM, OGDH (40-1046 aa) and the C-terminal of TCAIM (24-496 aa, without the N-terminal J domain) were expressed and purified from Rossetta star cells. The OGDH protein displayed the expected enzyme activity (Fig. 1E). The interaction between OGDH and TCAIM was confirmed *in vitro* using gel filtration. The peak volume of the OGDH-TCAIM complex was 58 mL, while that of OGDH was 65 mL, which was much smaller than that of the OGDH-TCAIM complex (Fig. 1F). An electrophoretic mobility shift assay (EMSA) was also carried out to test OGDH and TCAIM binding. OGDH could completely bind TCAIM at a molar ratio of 1:2 (Fig. 1G). These *in vitro* results indicated that the binding between TCAIM and OGDH was direct.

### TCAIM influences mitochondrial function and metabolism

TCAIM was identified as a “T cell activation inhibitor, mitochondrial” but its biochemical function has not been fully clarified<sup>12,13</sup>. Given its specific binding to OGDH, a subunit of the OGDHC enzyme complex, we reasoned that it would affect mitochondrial function. Indeed, overexpression of TCAIM changed mitochondrial morphology, displayed a more fragmented network (Fig. 2A), and decreased the maximum oxygen consumption rate (OCR) (Fig. 2B, Fig S2A), which is similar to the effect of OGDH knockdown (Fig S2 C-D). Surprisingly, the decrease in mitochondrial respiration was coupled with increased membrane potential and elevated mitochondrial ROS generation, as determined by JC-1 and MitoSOX staining, respectively (Fig. 2C and 2D). These results indicated that TCAIM decreases oxidative phosphorylation by suppressing electron transport chain (ETC) but profoundly affect energy metabolism. Similarly, overexpression of TCAIM also led to a decrease in the maximum extracellular acidification rate (ECAR) capacity, indicating that glycolysis was also affected by TCAIM overexpression (Fig. 2E, Fig S2E).

## Loss of TCAIM-altered metabolism in mice

To further investigate the biological function of TCAIM, we established a *Tcaim* knockout (KO) mouse model using CRISPR/Cas9 and validated the deletion of *Tcaim* by sequencing and qPCR (Fig S3A and B). Compared to their wild-type (WT) littermates, these mice displayed reduced bodyweight, without a change in food intake (Fig. 3A and B). Consistent with these phenotypes, *Tcaim* KO mice exhibited increased oxygen consumption compared with WT mice, indicating an increased metabolic rate (Fig. 3C). The human protein atlas database showed that the liver and kidney are among the organs with the highest *Tcaim* expression levels (<https://www.proteinatlas.org/>), and our qPCR results also confirmed this (Fig S3C). Moreover, 24 h of fasting followed by 16 h of feeding caused an elevation in *Tcaim* expression in mouse livers (Fig. 3D). The fact that the *Tcaim* mRNA level is the highest in the kidney and liver prompted us to speculate that loss of *Tcaim* likely causes metabolic changes in serum. Indeed, the serum metabolome of *Tcaim* KO mice was significantly different (Fig. 3E and Fig S3D). Several glycerophospholipids, such as phosphatidylcholine, phosphatidylglycerol, and phosphatidic acid were at the top of the list of reduced metabolites in the serum of KO mice, and glycerophospholipid metabolism was the most enriched category by KEGG analysis (Fig. 3F, Fig S3E, and Table S2). We further confirmed the changes in lipid metabolism in mice by measuring cholesterol levels in mouse serum. In line with our metabolome results, compared with the serum from WT mice, the serum of *Tcaim* KO mice contained significantly less free and total cholesterol (Fig. 3G and H). Interestingly, we also observed that compared to WT mice, the protein malonylation level was significantly decreased in the liver of *Tcaim* KO mice, but not the protein acetylation or succinylation levels (Fig. 3I, Fig S3F). This increase in protein malonylation levels could be mimicked by treating cells with malonate to increase malonyl-CoA levels (Fig S3G). Since SIRT5 has been reported to regulate protein malonylation, we also tested whether SIRT5 expression was altered in *Tcaim* KO mice but found no difference in SIRT5 protein levels between WT and KO mice (Fig S3H).

**TCAIM displays little effect on OGDH and OGDHC enzyme activities in vitro**

The type I and type II DNAJ protein (DNAJA and DNAJB) families are usually involved in protein folding and refolding by recruiting HSP70 to their clients, while the functions of the type III DNAJ protein (DNAJC) family are rather diverse, with some of them exhibiting HSP70-independent functions<sup>14</sup>. We asked whether the specific binding between OGDH and TCAIM interferes with the enzymatic functions of OGDH and OGDHC. Adding TCAIM to purified OGDH *in vitro* slightly suppressed its maximum activity (V<sub>max</sub>) and decreased the K<sub>m</sub> for its substrate  $\alpha$ -KG (Fig. 4A and B, Fig S4A and B). Applying TCAIM to OGDHC *in vitro* had no obvious effect on V<sub>max</sub> or the  $\alpha$ -KG K<sub>m</sub> of OGDHC under different pH conditions, even though the OGDHC activities decreased with an increase in buffer pH value (Fig. 4C). Therefore, these results indicated that TCAIM does not directly regulate the activity of OGDH or OGDHC. Since some DNAJ proteins are involved in client folding and refolding under stress conditions<sup>15,16</sup>, we further tested whether TCAIM helps OGDH maintain its structure or function under heat stress. An increase in temperature decreased the activity of purified OGDH, but the application of TCAIM protein had no effect on its function (Fig. 4D, Fig S4D). Moreover, the presence of TCAIM did not affect the thermal stability of the OGDH protein *in vitro* (Fig. 4E), while overexpression of TCAIM in HEK293T cells also showed no effect on the thermal stability of the OGDH protein *in vivo* (Fig. 4F). Interestingly, TCAIM seemed to bind poorly to heat-inactivated OGDH (Fig S4E), suggesting that TCAIM may not recognize misfolded OGDH protein.

### **TCAIM reduces OGDH protein level and the activity of OGDHC *in vivo***

Next, we investigated whether TCAIM affects OGDHC activity *in vivo*. Transient or stable overexpression of TCAIM in HeLa or HEK293T cells significantly reduced the enzymatic activity of OGDHC (Fig. 5A-D). We also noticed a significant reduction in OGDH protein levels with transient overexpression of TCAIM in HeLa cells, whereas the OGDH protein level only slightly decreased in HeLa cells stably overexpressing TCAIM (Fig. 5E and Fig S5A). A similar pattern of OGDH protein levels was also observed in TCAIM transiently or stably overexpressed in HEK293T cells (Fig S5B and C). Combined with our *in vitro* findings (Fig. 4), these results suggested that the decrease in OGDHC activity is most likely due to the reduction of OGDH protein, but not a direct inhibition of the enzyme complex (Fig S5D-G). In line with these findings, OGDH protein levels, as well as the enzymatic activities of OGDHC, were significantly increased in liver lysates of *Tcaim* KO mice compared to WT mice (Fig. 5F and G). We wondered whether TCAIM overexpression affects the proteome of mitochondria and decreases the levels of other mitochondrial proteins. To test this possibility, we examined the other two subunits of OGDHC, as well as irrelevant proteins, such as SIRT3, PHB1, and COX4. The levels of the tested mitochondrial proteins remained unchanged, with the exception of DLST, the E2 subunit of OGDHC, was also reduced in HeLa cells. Similarly, we did not observe an increase in the protein levels of the other tested candidates in liver lysates of *Tcaim* KO mice, compared to those of WT mice (Fig. 5F and Fig. 5H).

## **Single particle cryo-EM resolves the binding between TCAIM and native OGDH**

Since TCAIM binds to functional OGDH *in vivo* and *in vitro*, and this binding has little effect on OGDH function directly, but rather mediates OGDH degradation, we decided to elucidate how TCAIM binds to native OGDH. To evaluate how OGDH interacts with TCAIM, we established the structure of the TCAIM-OGDH complex using single-particle cryo-EM at an overall resolution of 2.86 Å (Fig S6A-C, Table S3).

With apoOGDH (hsOGDH only, PDB: 7WGR, Fig. 6A) structure modelling and alpha-fold predicted TCAIM structure modelling, we built an atomic model of the hsOGDH-TCAIM complex (Fig. 6B). In the hsOGDH-TCAIM complex, OGDH presented a configuration similar to that of apoOGDH, while TCAIM was depicted as a triangle lying on the  $\alpha/\beta 1$  domain of one molecule of the OGDH dimer (Fig. 6B). TCAIM adopts a three-repeat  $\alpha\beta\beta\beta$ -fold conformation, with one  $\alpha\beta\beta\beta$  following a long  $\alpha$  helix. The first and second repeats closely interacted with OGDHa (Fig. 6C/F). Among these binding sites, the C-terminal beta-strand (aa 467-490) displayed the closest binding distance to the surface of OGDHa and formed a hydrogen bond between Ser453 of TCAIM and Glu399 of OGDH (Fig. 6D). This binding site in TCAIM is conserved among different species, from *Drosophila* to humans (Fig. 6G and Fig S6D). In addition, Glu399 in OGDH homologues is conserved between *Drosophila* and humans (Fig. 6H).

In the hsOGDH-TCAIM complex, the density of the cofactor TPP and Mg<sup>2+</sup> could be clearly observed in the predicted TPP binding pocket compared to apoOGDH (Fig. 6C). In the pocket, well-defined Mg<sup>2+</sup> ions were coordinated with the side chains of Asp430 and Asn463, which are conserved in OGDH homologues.

We asked whether the binding of TCAIM affects the structure of OGDH and compared the structures of the OGDH dimer and the TCAIM-bonded OGDH dimer. No obvious difference was observed between these two structures with a RMSD of 0.3 Å (Fig. 6E). This result suggests that the binding of TCAIM alone does not change the structure of OGDH, nor does it rely on conformational changes in OGDH.

## **TCAIM mediates OGDH degradation in a mtHSP70-dependent manner**

We next aimed to decipher the mechanism by which TCAIM downregulates the protein level of OGDH. We first checked the mRNA level of OGDH in TCAIM transiently overexpressing HeLa cells compared to that of EGFP transiently overexpressing cells (Fig. 7A), and the mRNA level of *Ogdh* from the livers of *Tcaim* KO mice and their WT littermates (Fig. 7B). We found that the mRNA level of *OGDH* showed no significant change in either case, and thus, the change in transcription could not be the cause of the decrease in OGDH protein levels regulated by TCAIM.

Thus, we examined the mechanism by which TCAIM mediates the degradation of OGDH. Because TCAIM is a DNAJ protein, we first tested whether mitochondrial HSP70 (HSPA9) is necessary for TCAIM-mediated OGDH degradation. Indeed, HSPA9 knockdown attenuated the OGDH reduction (Fig. 7C). Moreover, the knockdown of LONP1 slightly attenuated the effect of TCAIM (Fig. 7D), but not knockdown of AAA Proteases CLPP or AFG3L2 (Fig S7A&B). Interestingly, applying 20 S protease inhibitor, MG132 also failed to attenuate the degradation of OGDH, indicating this mechanism is likely through a 20S

proteasome independent pathway (Fig S7C). These results indicate that the degradation of OGDH mediated by TCAIM may depend on the LON protease system, but not on the ubiquitination and CLP protease systems.

From our structural data, the last three beta-sheets of TCAIM displayed the closest distance to the surface of OGDH, indicating that this region may be responsible for TCAIM-OGDH binding. To test this hypothesis, we transiently overexpressed TCAIM mRNA that lacks this region (C-terminal beta sheet deletion CBD-TCAIM) to evaluate its effect on OGDH protein levels. Based on the prediction by Alphafold<sup>17</sup>, lack of this region does not cause dramatic structure change (Fig S7D). However, the absence of this region significantly reduced the interaction between TCAIM and OGDH and abolished the effect of TCAIM on the protein level of OGDH (Fig. 7E-F). Moreover, the absence of this region significantly attenuated the ability of TCAIM to reduce the maximum oxygen consumption rate in HeLa cells (Fig. 7G & Fig S7E).

## Discussion

The mitochondrial proteostasis system plays an important role in maintaining mitochondrial function and ageing<sup>18</sup>. In this study, we found that TCAIM, a novel DNAJ/Hsp40 protein, regulated metabolism, especially mitochondrial functions and lipid metabolism, at the cellular and organismal levels. Interestingly, TCAIM specifically targeted and mediated the degradation of native OGDH in a HSPA9-LONP1-dependent way. This finding suggests that besides maintaining the mitochondrial proteome and functions, the proteostasis system may also be directly involved in metabolic regulation, probably through selective degradation of native metabolic enzymes.

The OGDHC protein complex plays a unique and important role in the TCA cycle, as it is one of the rate-limiting enzymes of the citric acid cycle, and has also been reported to be the major site of ROS generation in the TCA cycle<sup>19</sup>. Moreover, its substrate,  $\alpha$ -ketoglutarate, links the TCA cycle and glutamine/amino acid catabolism and serves as an essential substrate for epigenetic modification<sup>20</sup>. However, in addition to allosteric regulation by its cofactors, substrates, and products, little is known about its post-translational regulation. We previously reported that its activities can be regulated by lysine acetylation, indicating the post-translational regulation of this enzyme<sup>10</sup>. In this study, we revealed a novel post-translational regulatory mechanism that determines the protein level of the E1 subunit of the OGDHC complex, and consequently affects the *in vivo* activity of this enzyme.

TCAIM was originally identified as a T-cell activation inhibitor by Sawitzki and colleagues, as its expression level was significantly reduced during T-cell activation<sup>12,13</sup>. A recent publication also reported a profound impact of TCAIM knock-in (KI) on T cell metabolism<sup>21</sup>. However, changes in TCAIM expression are coupled with changes in the expression of many genes involved in glycolysis, TCA cycle, and other metabolic pathways. These sequential modifications in metabolic gene expression may compensate for and even reverse the primary function of TCAIM in metabolism. Therefore, it is not surprising that they observed that TCAIM KI inhibited cholesterol biosynthesis gene expression, but the serum cholesterol level decreased in our KO mouse<sup>21</sup>. Nevertheless, consistent with the decrease in serum

cholesterol levels, the protein malonylation level was also reduced in the liver lysates of TCAIM KO mice. Malonyl-CoA is a unique precursor of fatty acid synthesis<sup>22</sup>, and increasing malonyl-CoA levels by applying malonate leads to an increase in protein malonylation levels. Therefore, even though it is indirect, the protein malonylation level may reflect the malonyl-CoA level in the liver cells and indicate a change in lipid biosynthesis.

TCAIM contains a J domain structure as well as an HPD motif after its mitochondrial leading sequence, but it is not followed by a glycine/phenylalanine-rich domain. Further studies revealed that it binds to the mitochondrial Hsp70 (mtHsp70) homologue, HSPA9. Moreover, its regulatory function is dependent on the presence of HSPA9. Taken together, our data suggested that TCAIM belongs to the type III DNAJ protein or DNAJC family. Unlike the members of type I or type II DNAJ protein families, DNAJC proteins display diverse functions and do not seem to bind non-native clients<sup>14</sup>. TCAIM also displays a similar aspect: *in vitro* binding assays as well as cryo-EM results show that it binds to native and functional OGDH, while its binding to heat-inactivated OGDH decreases significantly. The binding of DNAJC proteins to their mature, folded proteins play roles, such as “remodeling” of large multiprotein complexes and affecting the stability of protein–protein interactions<sup>23,24</sup>. But to our knowledge, DNAJ proteins have not been reported to drive protein degradation through direct target recognition as TCAIM does. However, we cannot eliminate the possibility that protein complexes of the OGDHC will be remodeled, followed by the degradation of OGDH, a replaceable E1 subunit of this protein complex<sup>25,26</sup>.

Recent studies have shown that DNAJ protein could assist the degradation of substrates of E3 ubiquitin ligase by stabilizing the ligase or by enhancing the binding between the ligase and substrate<sup>27,28</sup>. These regulations of protein degradation by the DNAJ protein are indirect; recognition and degradation of target proteins depend on the traditional E3 ubiquitin-protein ligase complex, not on the DNAJ protein *per se*. Thus, in contrast to TCAIM-OGDH regulation, the DNAJ proteins in these two studies are indirectly involved in protein degradation and are not essential for recognition or degradation of the target proteins.

The mitochondrial HSP70 protein plays several important roles in mitochondrial proteostasis. It is essential for the import and folding of mitochondrial precursor proteins<sup>29</sup>; it also promotes the degradation of misfolded proteins with the help of LONP1<sup>30</sup>. Although not found in mitochondria, cytosolic HSP70 protein facilitates the degradation of protein aggregates<sup>31</sup>. Therefore, it may not be surprising that we found that mtHSP70 plays a role in TCAIM-mediated OGDH degradation, that is mtHSP70 can facilitate its degradation of the native protein OGDH using TCAIM to recognize the target. LONP1 is an AAA + (ATPase associated with a variety of cellular activities) protease in the mitochondrial matrix and plays multiple roles in maintaining the mitochondrial proteome<sup>32,33</sup>. Recent research has also shown that it cooperates with the mtHSP70 chaperone system to assist mitochondrial protein folding<sup>34</sup>. Currently, there is no specific inhibitor of LONP1. The peptide aldehyde MG132 is one of the best inhibitors of Lon protease, but it is much more effective against the 20S proteasome and inhibits protein degradation via the ubiquitin-proteasome pathway<sup>9,35,36</sup>. Although several studies have found that MG132 can inhibit LONP1 function, the mechanism of action of MG132 on LONP1 is unclear, and the

inhibitory effect appears to be substrate dependent<sup>33,37</sup>. We did not observe any inhibitory effect of MG132 on OGDH degradation up to 40  $\mu\text{M}$ , which had a deleterious effect under our cell culture conditions. Nevertheless, LONP1 plays a role in TCAIM-mediated degradation of OGDH and most likely functions downstream of mtHSP70 as a protease.

Selective protein degradation is a key mechanism of post-translational regulation in cells, and plays an important role in various biological processes, particularly signal transduction<sup>38,39</sup>. In mitochondria, protein degradation is likely to affect metabolism because mitochondria are a crucial hub for metabolites. However, little is known about whether this protein degradation can serve as a specific regulation of certain metabolic pathways, or whether it can only globally impact all metabolism occurring in the mitochondria. This study demonstrated that TCAIM can specifically target and mediate degradation of OGDH, highlighting the importance of specific regulation of metabolism through selective protein degradation, and raising the possibility that the DNAJC family proteins may play an important role in this type of post-translational regulation of mitochondrial metabolism. Moreover, overexpression of the DNAJC protein could specifically target and mediate the degradation of a client protein, which could become a novel strategy for targeted protein degradation.

Several questions need to be addressed in the future. We found that refed after fasting upregulated TCAIM expression, suggesting that TCAIM may play a role in the regulation of nutrient metabolism. However, we still lack direct evidence regarding the circumstances or stress conditions in which this mechanism is regulated and becomes essential. We tested different tissue culture conditions, including low and high glucose levels, with or without glutamine, and applying a pro-oxidant or antioxidant. None of these modified the effect of TCAIM on OGDH in TCAIM-overexpressing cells (data not shown). Moreover, even though CompPASS analysis is good at identifying specific interacting proteins by reducing false positive data in IP-mass spectrometry experiments, it may remove real specific interactions<sup>10,40</sup>. Therefore, despite our data demonstrating that OGDH is the most specific interacting protein of TCAIM, we cannot eliminate the possibility that TCAIM has more binding proteins than OGDH and regulates their functions through a similar protein degradation mechanism or through completely different pathways.

In conclusion, the present study demonstrated that the mitochondrial proteostasis system could specifically regulate metabolism mediated by the DNAJC protein TCAIM by specifically binding to native OGDH and driving its degradation in a HSPA9-LONP1-dependent manner. This finding not only highlights a novel function of mitochondrial proteostasis in metabolism but also indicates a new field of DNAJC-mediated post-translational regulation of native proteins. Moreover, the potential of this new native protein degradation mechanism should be further explored in basic and translational research.

## Methods

### Cell Lines and Reagents

HEK 293T and HeLa cell lines were acquired from ATCC and cultured in DMEM/high glucose (HyClone, Logan, UT, USA) supplemented with 10% fetal bovine serum (FBS; Gibco, Waltham, MA, USA), 100 U/mL penicillin, and 100 mg/mL streptomycin (basal media, Shanghai, China). All cell lines tested negative for *Mycoplasma*. Cells were grown in a humidified incubator at 37 °C with 5% CO<sub>2</sub>.

## Antibodies

Anti-OGDH Antibody (Proteintech 15212-1-AP); Anti-malonyllysine antibody (PTM-Biolabs PTM-901); LONP1 Polyclonal Antibody (Proteintech 15440-1-AP); GRP75 Polyclonal Antibody (Proteintech 14887-1-AP); CLPP Polyclonal Antibody (Proteintech 15698-1-AP); AFG3L2 Antibody (Proteintech 14631-1-AP); HA(C29F4) Antibody (CST 3724S); GAPDH Antibody (Proteintech 600004); SIRT5 Antibody (Sigma HPA022002); Anti-Succinyllysine Mouse mAb (PTM-Biolabs PTM-419); SIRT3 (D22A3) Rabbit mAb (CST CST5490S); DLD Antibody (Abclonal A13296); DLST Antibody (Abclonal A13297);  $\beta$ -actin Antibody (Proteintech 66009); COX4I1 Antibody (CST 4844); MCL1 Polyclonal antibody (Proteintech 16225-1-AP); and Acetylated-Lysine Antibody (CST 9441S). All primary antibodies were used in 1:1000 dilution

## Plasmid construction and transfection

cDNA encoding h *TCAIM* and h *HSPA9* was subcloned into the pHAGE-C-HA-Puro lentivirus vector for *TCAIM*-HA or *HSPA9*-HA overexpression<sup>40</sup>. Lentiviruses were generated by transfection with the target or negative control vectors using the packaging plasmid mix and a ratio of 1:2 polyethyleneimine (PEI) (Polyscience, USA) into 293T cells. Pseudovirus was harvested 48 h later, filtered, and used to transduce HeLa cells in the presence of 10  $\mu$ g/mL polybrene. Infected HeLa cells were maintained in 1  $\mu$ g/ml puromycin for three days and expanded to perform the experiments. Transfection efficiency was confirmed by western blotting.

## SiRNA transfections

The siRNA sequences used to knock down *HSPA9*, *LONP1*, *CLPP*, and *AFG3L2* were: si *HSPA9* 5'-GCACAUUGUGAAGGAGUUCAATT-3'.

si *LONP1* 5'-CGAGAACAAGAAGGACUUCUATT-3';

si *CLPP* 5'-GCUCAAGAAGCAGCUCUAUAATT-3';

si *AFG3L2* 5'-GAGUAGUAGACAGAUUGGAAGUCGU-3'.

All siRNAs were synthesized by Hema Biotech (Shanghai, China). siRNA (50nM) transfection was performed using Lipofectamine 2000 (Thermo Scientific, Waltham, MA, USA) and Opti-MEM (Gibco, Waltham, MA, USA), according to the manufacturer's protocols. Cells were harvested 3–4 days after transfection.

## Plasmid construction

The plasmids used for the production of recombinant His-Sumo-OGDH (40-1026), His-SUMO-TCAIM (24-496) and His-SUMO-TCAIM (144-496) were constructed as follows. Total RNA was isolated from HEK 293T cells using TRIzol (TianGen, Beijing, China) and reverse-transcribed into cDNA using HiScript III RT SuperMix (Vazyme, Nanjing, China). cDNAs of OGDH (121-3078 bp), TCAIM (73-1488 bp), and TCAIM (433-1488 bp) were amplified by polymerase chain reaction (PCR) and cloned into the pet-28a-His-Sumo plasmid using the Gibson assembly clone with the Hieff Clone® Plus One Step Cloning Kit (Yeasen, Shanghai, China). The sequences were confirmed by DNA sequencing. The recombinant plasmids were transformed into *Escherichia coli* strain Rosetta (DE3) star for protein expression.

## Real-time PCR

Total RNA was isolated from prepared cell samples using TRIzol (TianGen, Beijing, China) and reverse-transcribed into cDNA using HiScript III RT SuperMix (Vazyme, Nanjing, China) according to the manufacturer's instructions. Quantitative PCR was performed using the LightCycler480 apparatus (Roche, Basel, Switzerland) using SYBR Green Master Mix (Yeasen, Shanghai, China). The primers used for real-time PCR are below. GAPDH was used as the internal control. Relative gene expression data were analyzed using the  $2^{-\Delta\Delta CT}$  method.

mTcaim-F GGCGAGAGAAAACATGACTAGAAGG

mTcaim-R CCATCTGTCTGCTAGAAATGCTGG

mOGDH-F CAAACCAGCAGCAATTAGGACG

mOGDH-R TGGGATTCTCCAACCAGGCA

mGAPDH-F AGGTCGGTGTGAACGGATTTG

mGAPDH-R TGTAGACCATGTAGTTGAGGTCA

**OGDH-F TTGGCTGGAAAACCCCAAAG**

**OGDH-R TGTGCTTCTACCAGGGACTGT**

**GAPDH-F CTGGCCAAGGTCATCCATGAC**

**GAPDH-R CTTGCCACAGCCTTGGCAG**

## Western blot

For immunoblotting, cells were lysed in mammalian cell lysis buffer (MCLB) (50 mM Tris pH 7.5, 150 mM NaCl, 0.5% IGEPAL® CA-630 (Sigma-Aldrich, I3021, USA)) for 30 min on ice, and the protein concentrations were determined by Bradford assay. Equal amounts of protein were separated by 10%

SDS polyacrylamide gel electrophoresis and transferred to nitrocellulose filter membranes (Millipore, USA). After blocking with 5% skim milk in TBST (50 mM Tris-HCl at pH 7.4, 150 mM NaCl, and 0.1% Tween 20), the membranes were incubated with the appropriate primary antibodies. Signals were detected using horseradish peroxidase (HRP)-conjugated secondary antibodies and an enhanced chemiluminescence (ECL) detection system (Sage Creation Science).

## Immunoprecipitation and mass spectrometry

293T cells were lysed at 4 °C in lysis buffer (50 mM Tris, pH 7.5, 150 mM NaCl, 0.5% NP40, supplemented with 1 mM PMSF, and complete EDTA-free protease inhibitor cocktail). Proteins in supernatant were separated by centrifugation (4 °C, 12,000 × *g*) for 20 min. The supernatant fractions were saved as loading input controls. Supernatants were subjected to immunoprecipitation with HA magnetic beads (Thermo Scientific, Waltham, MA, USA) overnight at 4 °C. The beads were then washed five times with lysis buffer and then three times with PBS. Binding proteins were eluted with a 0.1 M glycine solution, pH 2.0. Partially eluted samples were pre-processed and injected into a Q Exactive Plus mass spectrometer (Thermo Scientific, Waltham, MA, USA) coupled with an EASY-nLC 1000 liquid chromatography instrument (Thermo Scientific, Waltham, MA, USA). Bioinformatics and statistical analyses of the original mass spectrometric data were performed using Mascot (Matrix Science, London, UK; version 2.4.1) based on the uniprot\_human database (88,625 entries). Scaffold (version Scaffold\_4.2.1, Proteome Software Inc., Portland, OR) was used to validate MS/MS-based peptide and protein identification using the Scaffold Local FDR algorithm. Protein identification was accepted if it could be established at a probability greater than 95.0%. Protein probabilities were assigned using a protein probe algorithm. Proteins that contained similar peptides and could not be differentiated by MS/MS analysis alone were grouped to satisfy the principles of parsimony. Proteins that shared significant peptide evidence were grouped into clusters.

## Preparation of chemically modified mRNA

cDNA encoding h *TCAIM* was amplified from the pSUMO-TCAIM vector with primers TCAIM-F-pSG5L 5'-aagagccaccATGTTTTGCCACCTGAGACCTATG-3' and TCAIM-R-pSG5L 5'-gtacgggtaCTTAATGGCTTCTCCATTCTTCCAAT-3' by PCR and subcloned into the pSG5L vector flanking 5' and 3' UTRs and downstream of a T7 promoter using the Hieff Clone® Plus One Step Cloning Kit (Yeasen, Shanghai, China). The pSG5L-MLS-EGFP vector was optimized using the primers MLS-EGFP-R 5'-CTTGCTCACCATGAAAAGGGAAACCAGTGTGGAAATATC-3' and MLS-EGFP-F 5'-GGTTCCCTTTTCAATGGTGAGCAAGGGCGAGGAGC-3' on pSG5L-EGFP vector. TCAIM-HA and MLS-EGFP mRNAs were synthesized *in vitro* using T7 polymerase-mediated RNA transcription. DNA templates were amplified by PCR, purified, and used for *in vitro* transcription (IVT). The Cap1 analog (EzCap AG, B8176, APEX BIO, TX, USA) was included in the IVT reaction to place a cap 1 structure at the 5' end of the mRNAs. All mRNAs were synthesized using the full substitution of uridine (U) for the modified uridine analog N1-methyl-pseudouridine ( $m^1\psi$ ). Following transcription, a poly(A) tail was added to the RNA transcripts using a poly(A) tailing kit (K1053, APEX BIO, TX, USA). The mRNA was purified using the MEGAclear kit (AM1908, Thermo Fischer Scientific).

# Transfection of mRNA

Cells were seeded in a 6-well-plate to 70-90% confluency and transfected with 1-2  $\mu\text{g}/\text{well}$  mRNA using Lipofectamine 2000 (11668019, Thermo Fischer Scientific). Complexes at an mRNA ( $\mu\text{g}$ ) to reagent ( $\mu\text{l}$ ) ratio of 1:2 were prepared for most cell lines.

## Cellular thermal shift assay

Cultured HEK 293T cells overexpressing TCAIM-HA or empty vector were lysed in mammalian cell lysis buffer (MCLB) (50 mM Tris pH 7.5, 150 mM NaCl, 0.5% IGEPAL® CA-630 (Sigma-Aldrich, I3021, USA)) containing a complete EDTA-free protease inhibitor cocktail for 30 min on ice. Supernatant was separated by 12000 x  $g$  centrifugation for 20 min at 4 °C. After determination of protein concentrations by Bradford, supernatants were aliquoted into 6 tubes per 25  $\mu\text{g}$  (20  $\mu\text{L}$ ) and heat-treated at different temperatures (4, 40, 45, 50, 55, 60 °C) for 3 min. Heated lysates were separated via 12,000 x  $g$  centrifugation for 20 min at 4 °C. Supernatants (20  $\mu\text{L}$ ) were transferred and denatured with protein-loading dye, while pellets were completely dissolved in 20  $\mu\text{L}$  protein-loading dye. All of them were heated at 95 °C for 10 min. Equal volumes of the supernatant or pellet were separated using 10% SDS PAGE gels. The protein levels of OGDH, TCAIM, and GAPDH in the supernatant and pellet were detected by western blotting.

## Protein thermal shift assay

2.5  $\mu\text{M}$  purified OGDH protein or OGDH-TCAIM complex protein was mixed with 20  $\mu\text{L}$  of 5 x SYPRO Orange (Sigma S5692). Three replicate samples from each group were added to a Roche qPCR white bottom plate and transferred to a Roche Light Cycler 480 instrument. Heating rate of 0.06 °C/s was set to detect the melting curve of the target protein at 25-95 °C. The  $T_m$  value was analyzed using Light Cycler® Thermal Shift Analysis software.

### In vitro OGDH activity

OGDH activity was measured by 2,6-dichlorophenolindophenol (DCPIP) reduction rate at 610 nm in a reaction with 60  $\mu\text{g}$  OGDH, 50 mM  $\text{KH}_2\text{PO}_4$  (pH 7.5), 0.5 mM thiamine pyrophosphate (ThDp), 1.0 mM  $\text{MgCl}_2$  and 0.08 mM DCPIP at 37 °C. After equilibrating in a microplate reader (SYNERGY H1, BioTek) for 3-5 min, 2 mM  $\alpha$ -ketoglutarate was added to three replicate mixtures to initiate the reaction, and the final volume was 200  $\mu\text{L}$ . OGDH activity is shown as the DCPIP reduction rate based on the enzyme kinetics curve at 610 nm for the first 5 min. For the heated OGDH assay, 2  $\mu\text{M}$  OGDH was preheated at 42 or 45 °C for 10 min and then incubated with 10  $\mu\text{M}$  TCAIM or BSA protein for 10 min. BSA and TCAIM proteins alone were negative controls. For the TCAIM heat-inactivation assay, 10  $\mu\text{M}$  TCAIM was preheated at 60 °C for 10 min and added to the OGDH activity assay system to evaluate its effects on OGDH activity.

For  $K_m$  and  $V_{max}$  of the OGDH assay, 2  $\mu\text{M}$  OGDH was incubated with or without 10  $\mu\text{M}$  TCAIM for 20 min in advance. The OGDH activity was measured at different concentrations of  $\alpha$ -ketoglutarate. The initial velocity ( $V_0$ ) at different concentrations of  $\alpha$ -ketoglutarate was analyzed using Prism for  $K_m$  and  $V_{max}$  values.

## In vitro OGDHC activity

OGDHC activity was measured by the NADH (reduction product of  $\text{NAD}^+$  catalyzed by OGDHC) production rate at 344 nm excitation and 460 nm emission. 3.75 mU OGDHC (Sigma) was added to the reaction containing 0.312 mM  $\text{MgCl}_2$ , 0.125 mM EGTA, 0.0125% Triton X-100, 62.5 mM MOPS (pH 7.4), 7.5  $\mu\text{M}$   $\text{CaCl}_2$ , 6 mM Diethyl malonate, 2  $\mu\text{M}$  Rotenone and 2 mM  $\text{NAD}^+$  at 37 °C. When equilibrated in a 96 well block with a clear bottom plate (Corning) for 3-5 min, the reaction was initiated by the addition of 10 mM  $\alpha$ -ketoglutarate and 0.2 mM CoA to 200  $\mu\text{L}$  under continuous stirring. All samples were tested in triplicate. The autofluorescence signal of NADH (344/460 nm) was measured using a microplate reader (SYNERGY H1, BioTek). OGDHC activity was shown as the NADH production rate based on the enzyme kinetics curve at 344/466 nm for the first 5 min. For the  $K_m$  and  $V_{max}$  of the OGDHC assay, 3.75 mU OGDHC was first incubated with or without 10  $\mu\text{M}$  TCAIM for 20 min on ice. The OGDHC activity was measured at different concentrations of  $\alpha$ -ketoglutarate.  $V_0$  at different concentrations of  $\alpha$ -ketoglutarate was analyzed using Prism for  $K_m$  and  $V_{max}$  values.

## OGDHC activity assay using cell lysate

293T cells and HeLa cells transfected with 2  $\mu\text{g}$  TCAIM mRNA were washed twice with PBS and collected with lysis buffer (50 mM Tris pH8.0, 150 mM NaCl, 1% Chaps, 1 mM PMSF, and complete EDTA-free protease inhibitor cocktail). The cells were lysed on ice for 20 min and the supernatant was separated by centrifugation (4 °C, 12,000  $\times g$ ) for 20 min. Protein concentrations were determined using Bradford assay. Whole cell lysate (20  $\mu\text{g}$ ) was added to the OGDHC activity system as the *in vitro* activity described previously. OGDHC activity was measured by the NADH production rate at 344 nm excitation / 460 nm emission from 4 mM  $\alpha$ -ketoglutarate. Normalized OGDHC activity was indirectly determined by the ratio of total enzyme activity to the OGDH protein expression level.

## Protein expression and purification

Recombinant OGDH and TCAIM strains were cultured at 37 °C in 2 L LB medium supplemented with 50  $\mu\text{g}/\text{mL}$  kanamycin and 35  $\mu\text{g}/\text{mL}$  chloramphenicol. Protein expression was induced at  $\text{OD}_{600} \approx 0.6$  by the addition of isopropyl  $\beta$ -D-1-thiogalacto-pyranoside (IPTG, final concentration 0.2 mM). The induced culture was incubated at 18 °C overnight. For OGDH purification, the cells were harvested by centrifugation and resuspended completely in lysis buffer (50 mM  $\text{KH}_2\text{PO}_4$  pH 7.5, 300 mM KCl, 0.5 mM ThDp, 25 mM imidazole pH 8.0, 1 mM PMSF + PI, 10 U/ml DNase I, 100  $\mu\text{g}/\text{ml}$  lysozyme; 1mM Vit B, 400  $\mu\text{M}$  TCEP). The resuspended cells were lysed under 900 MPa pressure using a JNBIO homogenizer (Guangzhou Juneng Biology & Technology Co., Ltd.). The homogenate was clarified by ultracentrifugation at 18,000  $\times g$ , and the supernatant was loaded onto a HisTrap™ HP column (GE Healthcare) and eluted with elution buffer (50 mM  $\text{KH}_2\text{PO}_4$  pH 7.5, 300 mM KCl, 0.5 mM ThDp, 500 mM imidazole pH 8.0) with a linear gradient. The fractions containing the recombinant His-Sumo-OGDH protein were pooled, digested with Ulp1 protease, and dialyzed against buffer S (50 mM  $\text{KH}_2\text{PO}_4$  pH 7.5, 300 mM KCl, 0.5 mM ThDp). The sample was loaded onto a HisTrap™ HP column to remove the cleaved His-Sumo tag. The flow-through containing the OGDH protein was concentrated and loaded onto

a HiLoad 16/60 Superdex<sup>TM</sup> 200 column (GE Healthcare) equilibrated with gel filtration buffer (20 mM  $\text{KH}_2\text{PO}_4$  pH 7.5, 300 mM KCl, 0.5 mM ThDp, 1mM  $\text{MgCl}_2$ , 400  $\mu\text{M}$  Tcep). Protein purity was analyzed by SDS-PAGE and Coomassie staining. Fractions containing the target protein were concentrated using an Amicon-Ultra-4 10K centrifugal device from Millipore, flash-frozen in liquid nitrogen, and stored at  $-80^\circ\text{C}$  until use.

For OGDH-TCAIM complex purification, the OGDH and TCAIM cell pellets were combined and resuspended in the lysis buffer above, followed by the same purification procedure. After Ulp1 protease digestion, the sample was loaded onto a HisTrap<sup>TM</sup> HP column twice and washed with 65 mM, 125 mM, 250 mM, and 500 mM imidazole (pH 8.0) separately. The OGDH-TCAIM complex was eluted in 125 mM imidazole (pH 8.0) and concentrated for gel filtration. The final concentration of OGDH and OGDH-TCAIM complex was 20 mg/mL.

## Electrophoretic mobility shift assays (EMSA)

The binding of OGDH and TCAIM was monitored by EMSA. OGDH (8  $\mu\text{L}$ ), TCAIM (8  $\mu\text{L}$ ), and binding buffer (4  $\mu\text{L}$ , 150 mM Tris-HCl pH 7.5, 150 mM NaCl, 25 mM  $\text{MgCl}_2$ , 5 mM DTT, 0.5 mM EDTA, 25% glycerol) were mixed in a thin-wall Eppendorf tube. The final concentration of OGDH was 2  $\mu\text{M}$ , and TCAIM was 1, 2, 4, 8, 12, or 16  $\mu\text{M}$ . The reaction mixture was incubated on ice for 20 min. Samples were loaded onto a pre-cooled 5% native polyacrylamide gel and were run at 110 V for 70 min at  $4^\circ\text{C}$  in  $0.5 \times$  TBE buffer. Protein bands were visualized using Coomassie Brilliant Blue staining.

## Sample preparation and cryo-EM data acquisition

Four microliters of freshly purified OGDH or OGDH-TCAIM144 at a concentration of 1.5 mg/mL was applied to glow-discharged 300-mesh Quantifoil R1.2/1.3 holey carbon grids (Quantifoil N1-C14nCu30-01). Grids were blotted for 3.0 s at  $4^\circ\text{C}$  and 100% humidity on an TFS Mark IV Vitrobot before being plunge-frozen in liquid ethane cooled by liquid nitrogen. Frozen OGDH grids were transferred to a TFS Titan Krios electron microscope (Thermo Fisher Scientific) operating at 300 kV, equipped with a Gatan BioQuantum energy filter (slit width 20 eV). Images were recorded using a K2 Summit direct electron detector in super-resolution mode. Data acquisition was performed using the SerialEM 3.8<sup>41</sup> with a nominal magnification of 165,000X, corresponding to a physical pixel size of 0.86  $\text{\AA}$ . The dose rate on the detector was  $\sim 8.0$  counts per pixel per second, with a frame exposure time of 0.175 s and a total exposure time of 5.6 s. Each micrograph stack contained 32 frames. The total dose rate was approximately  $60 \text{ e}^-/\text{\AA}^2$  for each micrograph. For the OGDH-TCAIM144, frozen grids were also loaded onto a TFS Titan Krios electron microscope (Thermo Fisher Scientific) operating at 300 kV, of which is equipped with a Gatan BioQuantum energy filter (slit width 20 eV) and a K3 summit direct electron detector. Images were collected in counting mode (Bin 0.5). Data acquisition was performed using an EPU with a nominal magnification of 105,000X, corresponding to a physical pixel size of 0.855  $\text{\AA}$ . The dose rate on the detector was  $\sim 20.0$  counts per pixel per second with a frame exposure time of 0.07 second and a total exposure time of 2.24 seconds. Each micrograph stack contains 32 frames. The total dose rate was approximately  $60 \text{ e}^-/\text{\AA}^2$  for each micrograph.

# Cryo-EM data processing

The drift correction of all image was performed using MotionCor2<sup>42</sup> with  $2 \times 2$  binning, and a dose-weighted sum of all frames from each movie was used for all image-processing steps. After whole-image CTF estimation using CTFFIND-4.1<sup>43</sup>, the remaining steps were performed using cryoSPARC<sup>44</sup>. Particles were auto-picked, and after several rounds of 2D classification, good particles were selected for further 3D analysis. These particles were used to generate initial models for 3D classification and 3D refinement. All refinements followed the gold-standard resolutions estimated based on the gold-standard Fourier shell correlation (FSC) = 0.143 criterion. The number of particles in each dataset and other details related to the data processing are summarized in Supplementary Fig S6 and Fig S7.

## Model building, refinement, and validation

Atomic models of OGDH and OGDH-TCAIM144 were manually built and adjusted using COOT<sup>45</sup>. The models were then subjected to global refinement and minimization in real-space refinement using PHENIX<sup>46</sup> with a secondary structure.

## Metabolic cage and bodyweight measurements

TCAIM heterozygous knockout mice were bred for two generations to obtain TCAIM homozygous knockout mice and wild-type littermates. All animals were raised in an SPF environment, and their bodyweight was recorded twice per week after weaning. They were transferred to the Comprehensive Lab Animal Monitoring System of Columbus Instruments at 4 mos of age to record the oxygen consumption rate and food intake over a 96 h period. The mean velocity of oxygen consumption ( $VO_2$ ) and daily feed were calculated for dark and light cycles. Animal experiments were conducted in accordance with institutional guidelines approved by the international Animal Care and Use Committee (IACUC) of Shanghai Jiao Tong University School of Medicine (Approval Code: A-2019-017, Approval Date:2019).

## Mitochondrial metabolism measurement using Seahorse instrument

The oxygen consumption rate was determined using an Agilent Seahorse XF Cell Mito Stress Test Kit (Agilent Technologies, USA, 103015-100), and glycolytic function was determined using an Agilent Seahorse XF Glycolysis Stress Test Kit (Agilent Technologies, USA, 103020-100). HeLa cells were plated at  $1 \times 10^4$  cells/well on a Seahorse XF Cell Culture Microplate (Agilent Technologies, USA, 102416-100). One hour before the assay, the medium was changed to 180  $\mu$ L/well of OCR XF base medium (Seahorse XF DMEM (Agilent Technologies, USA, 103575-100), 1 mM pyruvate, 2 mM glutamine, 25mM glucose; pH 7.4) or ECR XF base medium (Seahorse XF DMEM, 1 mM pyruvate, 2 mM glutamine; pH 7.4). The cell culture microplate was placed in a 37 °C non-CO<sub>2</sub> incubator for 1 h. Different compounds were loaded into the appropriate ports of a hydrated sensor cartridge (OCR: 2  $\mu$ M oligomycin, 0.75  $\mu$ M FCCP, 0.5 $\mu$ M Rotenone and antimycin A; ECR: 10mM glucose, 2 $\mu$ M oligomycin, 50mM 2DG). Oxygen respiration status

and pH change were then collected and analyzed using Agilent Seahorse XFe/XF analyzers, according to the manufacturer's instructions.

## ROS measurement

Cells were trypsinized, collected by centrifugation for 5 min at 500 x *g*, and then incubated with MitoSOX (5  $\mu$ M) (Thermo Scientific, USA, m36008) diluted in DMEM for 10 min at 37 °C. After staining, the cells were washed with PBS and analyzed using a BD FACSVerse™ Flow Cytometer with 510 nm excitation and 580 nm bandpass emission filters. The data were analyzed using FlowJo V10.

## Mitochondrial membrane potential

Cells were trypsinized, collected by centrifugation for 5 min at 500 x *g*, and then incubated with JC-1 (2  $\mu$ M) (Thermo Scientific, USA, M34152) diluted in DMEM for 30 min at 37 °C. After staining, the cells were washed with PBS and analyzed using a BD FACSVerse™ Flow Cytometer at 488 nm excitation with 527 nm and 586 nm bandpass emission filters. The data were analyzed using FlowJo V10.

## Mitochondrial morphology

Cells were seeded on vitreous cell culture to 30-50% confluence and then stained with 50nM MitoTracker Red (Thermo Scientific, USA) in DMEM for 30 min at 37 °C. After washing with PBS, the cells were recovered in complete media for 1 h, and images were acquired with a Leica DMI8 fluorescent microscope using a 100X oil lens.

## Mouse metabolomics analysis

Whole blood samples were collected from heart punctures, then incubated at room temperature for 1 h, followed by 10 min of centrifuging at 1000 x *g*. Serum was collected by carefully transferring the supernatant into tubes, and samples were stored at -80 °C until measurement.

300 $\mu$ L of Methanol (containing 5  $\mu$ g/mL 2-Chloro-L-phenylalanine as an internal standard) was added to 100 $\mu$ L of each serum and then mixed using a vortexer for 1 min. Then the mixture was centrifuged at 13,000 rpm, 4 °C for 10 min. The supernatant was then transferred to a sample vial for detection. An in-house quality control (QC) was prepared by mixing equal amounts of each sample and passing through a 0.45  $\mu$ m filter membrane.

An Agilent 1290 Infinity $\square$  UHPLC system coupled with an Agilent 6545 UHD and Accurate-Mass Q-TOF/MS was used for LC-MS analysis. The chromatographic column used was Waters XSelect HSS T3 (2.5  $\mu$ m 100\*2.1 mm).

Mobile phase A: Aqueous solution containing 0.1% formic acid. B: Acetonitrile solution containing 0.1% formic acid. The flow rate was 0.35 ml/min. Column temperature: 40 °C. The injection volume was 1  $\mu$ l in positive mode and 2  $\mu$ l in negative mode. The gradient elution conditions were optimized as follows: 0–2 min, 5% B; 2-10 min, 5-95% B; 10–15 min, 95% B. Post time was set as 5 min for system balance.

Mass spectrometry was performed in both positive and negative ion modes. The optimized parameters were as follows: Capillary voltage: 3.5 kV; drying gas flow: 10 l/min; gas temperature: 325 °C; nebulizer pressure, 20 psig; fragmentor voltage: 120 V; skimmer voltage: 45 V; mass range: m/z 50–3000.

## Dietary treatment, food intake

7 days prior to dietary treatment, mice were individually housed. Fasting for 20 h was accomplished by placing mice in a new cage without food and with *ad libitum* access to water. Refeeding entailed allowing fasted mice *ad libitum* access to normal chow for 8 h.

## Primary hepatocyte isolation and culture

Primary hepatocytes were obtained from 2-to 3-month-old mice. The mice were killed by carbon dioxide, and the thoracic and abdominal cavities were opened. A flow of perfusion buffer (HBSS without Ca/Mg, 0.75% NaHCO<sub>3</sub>, 0.06mM EDTA) began through the ventriculus sinister, and the portal vein was immediately cut. When the blood was removed, the liver was perfused with collagenase buffer (HBSS with Ca/Mg, collagenase type 2 (Worthing, USA, LS004176) (to light medium brown), 5mM CaCl<sub>2</sub>, 0.75% NaHCO<sub>3</sub>). Primary hepatocytes were resuspended in DMEM/high glucose, passed through a 70µm cell strainer, and centrifuged for 2 min at 520rpm. After another wash with DMEM/high glucose by centrifugation for 2 min at 520 rpm the resulting hepatocytes were plated in a 10 cm dish coated with collagen type I.

## Serum cholesterol measurement

Cholesterols were measured using a Cholesterol Assay Kit (Abcam ab65390) according to the manufacturer's instructions. Briefly, sera were obtained as described in the metabolomic analysis method, and low-density or very-low-density lipoprotein (LDL/VLDL) was separated from high-density lipoprotein (HDL) by precipitation and centrifugation. Free cholesterol was incubated without cholesterol esterase, while total cholesterol was obtained with cholesterol esterase in the assay buffer provided by the kit. After 37 °C reaction for 60 min, reaction mixtures were measured on a microplate reader (SYNERGY H1, BioTek) at Ex/Em: 535/587 nm. Concentrations were calculated based on the cholesterol standard curve.

## Data Availability

The datasets from this study are provided in the Supplementary Information/Source data file. The mass spectrometry proteomics data have been deposited to the ProteomeXchange Consortium via the PRIDE partner repository with the dataset identifier PXD030119. Structure model and cryo-EM density map files have been deposited in the in the Electron Microscopy Data Bank and Protein Data Bank under the accession numbers EMD-32496 and 7WH2, respectively.

## Declarations

## Acknowledgement

We thank all the members of Yang and Xu Labs for their insightful discussions. We thank Prof. Jinke Chen (School of Medicine, Shanghai Jiao Tong University) for his suggestions regarding manuscript preparation. Our proteomics and mass spectrometry analyses were performed at the Proteomics Platform of the Core Facility of Basic Medical Sciences, Shanghai Jiao Tong University School of Medicine (SJTU-SM). We thank all staffs at the Cryo-EM Center of Southern University of Science and Technology for their assistances. We gratefully acknowledge generous funding from the National Key Research and Development Program of China (2019YFA0508601) and National Natural Science Foundation of China (31871430 and 31900856).

## Author Contribution

W.J.H. designed and carried out all cytological and metabolism-related experiments, and also some of the molecular biology and mouse biochemistry experiments. Z.Y.H. carried out all mouse physiology experiments and part of the molecular and biochemical experiments. M.X.M. assisted with cryo-EM data acquisition. G.Y.Z. carried out the model building and refinement. Z.D.J. participated in 120 kV data acquisition. W.J. designed and performed all proteomic experiments and analyzed the proteomic data. F.Y.K. participated in mice and molecular biology experiments; H.Y.T assisted with biochemical experiments; Z.Y. assisted with mRNA preparation; S.F. assisted with mouse experiments; X.Y.J. contributed to designing cell biology experiments. W.P. contributed to the structural biology data acquisition and model building. Y.X. designed and carried out all the structural biology experiments and participated in designing and carrying out the molecular and biochemical experiments. Y.W. participated in designing all the experiments and data analysis. All authors were involved in data interpretation and contributed to writing the manuscript. Y.X., W.J.H. and Y.W. wrote the manuscript.

## References

1. Song, J., Herrmann, J.M. & Becker, T. Quality control of the mitochondrial proteome. *Nat Rev Mol Cell Biol* **22**, 54-70 (2021).
2. Vatrinet, R. *et al.* The alpha-ketoglutarate dehydrogenase complex in cancer metabolic plasticity. *Cancer Metab* **5**, 3 (2017).
3. Strumilo, S. Short-term regulation of the alpha-ketoglutarate dehydrogenase complex by energy-linked and some other effectors. *Biochemistry (Mosc)* **70**, 726-9 (2005).
4. Hipp, M.S., Kasturi, P. & Hartl, F.U. The proteostasis network and its decline in ageing. *Nat Rev Mol Cell Biol* **20**, 421-435 (2019).

5. Moehle, E.A., Shen, K. & Dillin, A. Mitochondrial proteostasis in the context of cellular and organismal health and aging. *J Biol Chem* **294**, 5396-5407 (2019).
6. Varshavsky, A. The Ubiquitin System, Autophagy, and Regulated Protein Degradation. *Annu Rev Biochem* **86**, 123-128 (2017).
7. Bota, D.A. & Davies, K.J. Lon protease preferentially degrades oxidized mitochondrial aconitase by an ATP-stimulated mechanism. *Nat Cell Biol* **4**, 674-80 (2002).
8. Pryde, K.R., Taanman, J.W. & Schapira, A.H. A LON-ClpP Proteolytic Axis Degrades Complex I to Extinguish ROS Production in Depolarized Mitochondria. *Cell Rep* **17**, 2522-2531 (2016).
9. Lavie, J. *et al.* Ubiquitin-Dependent Degradation of Mitochondrial Proteins Regulates Energy Metabolism. *Cell Rep* **23**, 2852-2863 (2018).
10. Yang, W. *et al.* Mitochondrial Sirtuin Network Reveals Dynamic SIRT3-Dependent Deacetylation in Response to Membrane Depolarization. *Cell* **167**, 985-1000 e21 (2016).
11. Dekker, S.L., Kampinga, H.H. & Bergink, S. DNAJs: more than substrate delivery to HSPA. *Front Mol Biosci* **2**, 35 (2015).
12. Schumann, J. *et al.* The mitochondrial protein TCAIM regulates activation of T cells and thereby promotes tolerance induction of allogeneic transplants. *Am J Transplant* **14**, 2723-35 (2014).
13. Vogel, S.Z. *et al.* TCAIM decreases T cell priming capacity of dendritic cells by inhibiting TLR-induced Ca<sup>2+</sup> influx and IL-2 production. *J Immunol* **194**, 3136-46 (2015).
14. Kampinga, H.H. & Craig, E.A. The HSP70 chaperone machinery: J proteins as drivers of functional specificity. *Nat Rev Mol Cell Biol* **11**, 579-92 (2010).
15. Agashe, V.R. *et al.* Function of trigger factor and DnaK in multidomain protein folding: increase in yield at the expense of folding speed. *Cell* **117**, 199-209 (2004).
16. Lu, Z. & Cyr, D.M. The conserved carboxyl terminus and zinc finger-like domain of the co-chaperone Ydj1 assist Hsp70 in protein folding. *J Biol Chem* **273**, 5970-8 (1998).
17. Mirdita, M. *et al.* ColabFold - Making protein folding accessible to all. *bioRxiv*, 2021.08.15.456425 (2021).
18. Kaushik, S. & Cuervo, A.M. Proteostasis and aging. *Nat Med* **21**, 1406-15 (2015).
19. Brand, M.D. Mitochondrial generation of superoxide and hydrogen peroxide as the source of mitochondrial redox signaling. *Free Radic Biol Med* **100**, 14-31 (2016).

20. Zdzisinska, B., Zurek, A. & Kandefer-Szerszen, M. Alpha-Ketoglutarate as a Molecule with Pleiotropic Activity: Well-Known and Novel Possibilities of Therapeutic Use. *Arch Immunol Ther Exp (Warsz)* **65**, 21-36 (2017).
21. Iwert, C. *et al.* TCAIM controls effector T cell generation by preventing Mitochondria-Endoplasmic Reticulum Contact Site-initiated Cholesterol Biosynthesis. *bioRxiv*, 2021.04.20.440500 (2021).
22. McGarry, J.D., Takabayashi, Y. & Foster, D.W. The role of malonyl-coa in the coordination of fatty acid synthesis and oxidation in isolated rat hepatocytes. *J Biol Chem* **253**, 8294-300 (1978).
23. Meyer, A.E., Hoover, L.A. & Craig, E.A. The cytosolic J-protein, Jjj1, and Rei1 function in the removal of the pre-60 S subunit factor Arx1. *J Biol Chem* **285**, 961-8 (2010).
24. Ungewickell, E. *et al.* Role of auxilin in uncoating clathrin-coated vesicles. *Nature* **378**, 632-5 (1995).
25. Leandro, J. *et al.* DHTKD1 and OGDH display substrate overlap in cultured cells and form a hybrid 2-oxo acid dehydrogenase complex in vivo. *Hum Mol Genet* **29**, 1168-1179 (2020).
26. Dai, W. *et al.* OGDHL silencing promotes hepatocellular carcinoma by reprogramming glutamine metabolism. *J Hepatol* **72**, 909-923 (2020).
27. Kim, H.Y., Kim, Y.M. & Hong, S. DNAJB9 suppresses the metastasis of triple-negative breast cancer by promoting FBXO45-mediated degradation of ZEB1. *Cell Death Dis* **12**, 461 (2021).
28. Wang, H. *et al.* DNAJC5 promotes hepatocellular carcinoma cells proliferation though regulating SKP2 mediated p27 degradation. *Biochim Biophys Acta Mol Cell Res* **1868**, 118994 (2021).
29. Craig, E.A. Hsp70 at the membrane: driving protein translocation. *BMC Biol* **16**, 11 (2018).
30. Wagner, I., Arlt, H., van Dyck, L., Langer, T. & Neupert, W. Molecular chaperones cooperate with PIM1 protease in the degradation of misfolded proteins in mitochondria. *EMBO J* **13**, 5135-45 (1994).
31. De Los Rios, P., Ben-Zvi, A., Slutsky, O., Azem, A. & Goloubinoff, P. Hsp70 chaperones accelerate protein translocation and the unfolding of stable protein aggregates by entropic pulling. *Proc Natl Acad Sci U S A* **103**, 6166-71 (2006).
32. Pinti, M. *et al.* Emerging role of Lon protease as a master regulator of mitochondrial functions. *Biochim Biophys Acta* **1857**, 1300-1306 (2016).
33. Bezawork-Geleta, A., Brodie, E.J., Dougan, D.A. & Truscott, K.N. LON is the master protease that protects against protein aggregation in human mitochondria through direct degradation of misfolded proteins. *Sci Rep* **5**, 17397 (2015).

34. Shin, C.S. *et al.* LONP1 and mtHSP70 cooperate to promote mitochondrial protein folding. *Nat Commun* **12**, 265 (2021).
35. Bayot, A. *et al.* Towards the control of intracellular protein turnover: mitochondrial Lon protease inhibitors versus proteasome inhibitors. *Biochimie* **90**, 260-9 (2008).
36. Frase, H., Hudak, J. & Lee, I. Identification of the proteasome inhibitor MG262 as a potent ATP-dependent inhibitor of the Salmonella enterica serovar Typhimurium Lon protease. *Biochemistry* **45**, 8264-74 (2006).
37. Sanchez-Lanzas, R. & Castano, J.G. Mitochondrial LonP1 protease is implicated in the degradation of unstable Parkinson's disease-associated DJ-1/PARK 7 missense mutants. *Sci Rep* **11**, 7320 (2021).
38. Lecker, S.H., Goldberg, A.L. & Mitch, W.E. Protein degradation by the ubiquitin-proteasome pathway in normal and disease states. *J Am Soc Nephrol* **17**, 1807-19 (2006).
39. Liu, H., Urbe, S. & Clague, M.J. Selective protein degradation in cell signalling. *Semin Cell Dev Biol* **23**, 509-14 (2012).
40. Sowa, M.E., Bennett, E.J., Gygi, S.P. & Harper, J.W. Defining the human deubiquitinating enzyme interaction landscape. *Cell* **138**, 389-403 (2009).
41. Mastronarde, D.N. Automated electron microscope tomography using robust prediction of specimen movements. *J Struct Biol* **152**, 36-51 (2005).
42. Zheng, S.Q. *et al.* MotionCor2: anisotropic correction of beam-induced motion for improved cryo-electron microscopy. *Nat Methods* **14**, 331-332 (2017).
43. Rohou, A. & Grigorieff, N. CTFFIND4: Fast and accurate defocus estimation from electron micrographs. *J Struct Biol* **192**, 216-21 (2015).
44. Punjani, A., Rubinstein, J.L., Fleet, D.J. & Brubaker, M.A. cryoSPARC: algorithms for rapid unsupervised cryo-EM structure determination. *Nat Methods* **14**, 290-296 (2017).
45. Emsley, P. & Cowtan, K. Coot: model-building tools for molecular graphics. *Acta Crystallogr D Biol Crystallogr* **60**, 2126-32 (2004).
46. Adams, P.D. *et al.* PHENIX: a comprehensive Python-based system for macromolecular structure solution. *Acta Crystallogr D Biol Crystallogr* **66**, 213-21 (2010).

## Figures

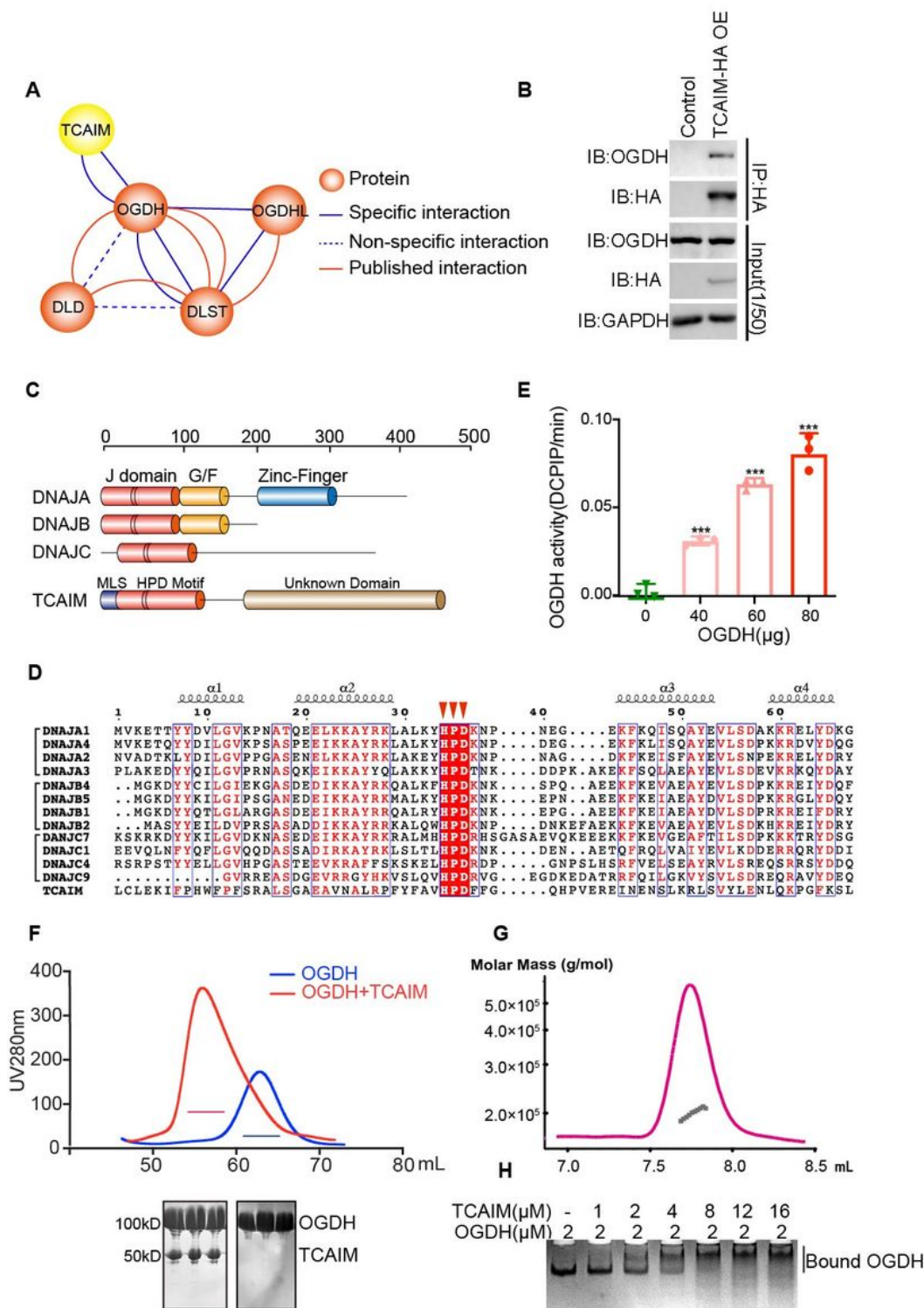


**Figure 1**

**TCAIM is a specific OGDH-interacting DNAJ protein**

**A.** Graphic demonstration of the interactions of TCAIM with subunits of OGDHC identified through co-immunoprecipitations (IP) using TCAIM-HA, OGDH-HA and DLST-HA as bait and analyzed by CompPASS.

- B.** Co-immunoprecipitations using TCAIM-HA as bait from the cell lysate of TCAIM-HA overexpression HEK293T cells as well as that of empty vector-transfected control HEK293T cells, and blotted with anti-OGDH, HA, or GAPDH antibodies.
- C.** Domain organization of DNAJ family proteins. Different domains were marked by different colors.
- D.** Sequence alignment of J domains in human DNAJ family members. The HPD motif is marked by an inverted triangle.
- E.** OGDH overexpressed in Rosetta DE3 *E. coli* was purified by His-tag resin and Superdex 200pg. DCPIP reduction rates taken from the enzyme kinetics curve at 600 nm for the first 5 minutes were calculated as OGDH activities of different protein amounts. (\*\*\*) $p < 0.001$ ).
- F.** Gel filtration of OGDH and OGDH-TCAIM complex. The SDS-PAGE result corresponds with the horizontal line.
- G.** EMSA assay of OGDH and TCAIM. Different concentrations of TCAIM were incubated with OGDH for 20 min and evaluated by native gel. The concentration is shown.

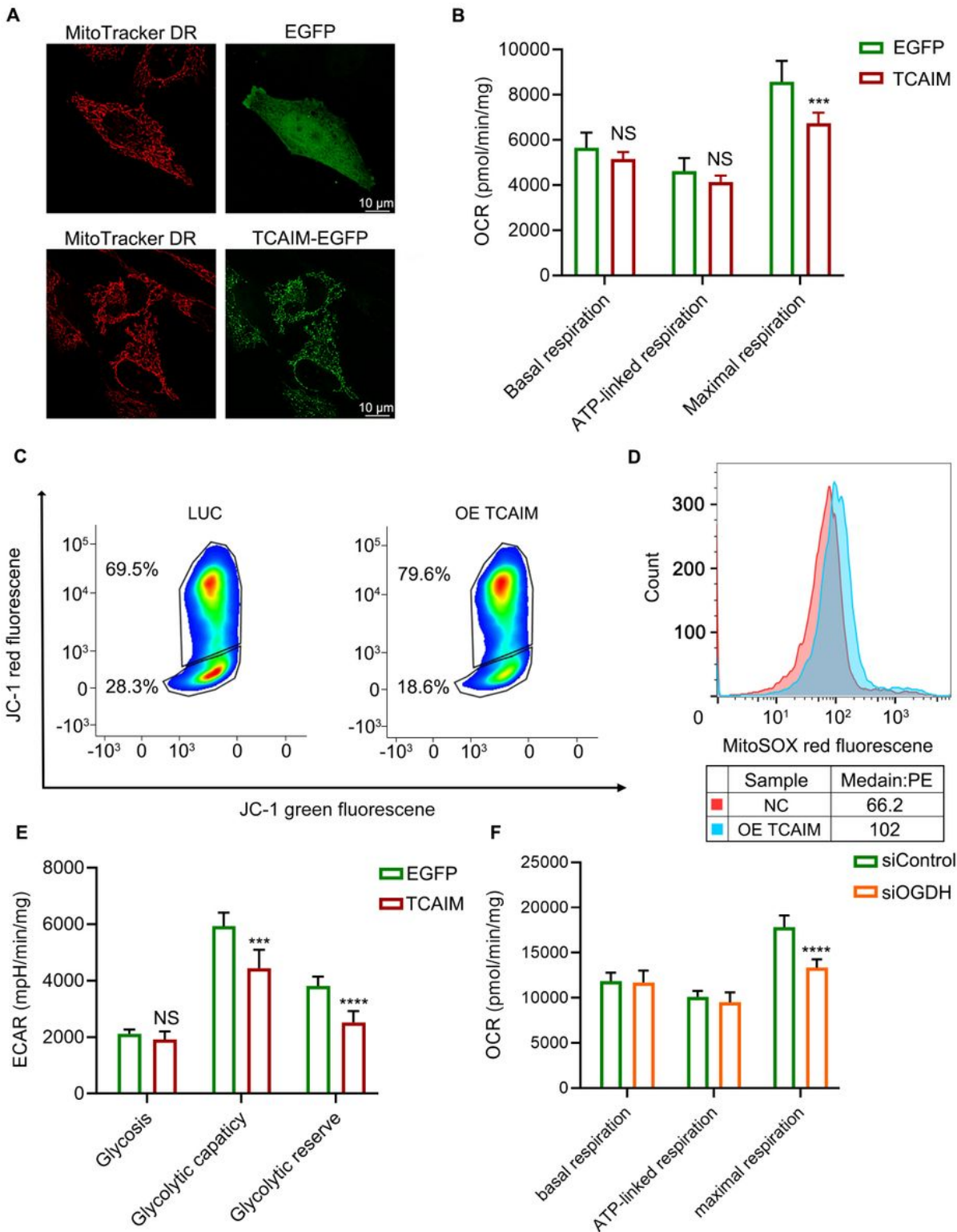


**Figure 2**

### TCAIM impacts mitochondrial function and metabolism

**A.** Fluorescence signal of HeLa cells which transiently overexpressed mitochondrial target EGFP or TCAIM-EGFP mRNA and stained with MitoTracker Deep Red, captured by Leica widefield microscope using 488 nm excitation with 507 nm emission.

- B.** The oxygen consumption rate (OCR) of HeLa cells which transiently over-expressed EGFP or TCAIM mRNA, collected by Seahorse instrument in serum-free basal DMEM containing 25 mM glucose and 4 mM glutamine.
- C.** HeLa cells transiently overexpressing TCAIM or LUCIFERASE were stained with JC-1 and analyzed by a flow cytometer using 488 nm excitation with 530/30 nm and 585/42 nm bandpass emission filters.
- D.** HeLa cells transiently overexpressing TCAIM or LUCIFERASE were stained with MitoSOX and analyzed by a flow cytometer using 510 nm excitation with 580 nm bandpass emission filters.
- E.** The glycolytic function of HeLa cells transiently overexpressing EGFP or TCAIM mRNA obtained by Seahorse in serum-free basal DMEM containing 4 mM glutamine.
- F.** The oxygen consumption rate (OCR) of HeLa cells with transiently knocked down OGDH collected by Seahorse in serum-free basal DMEM containing 25 mM glucose and 4 mM glutamine.

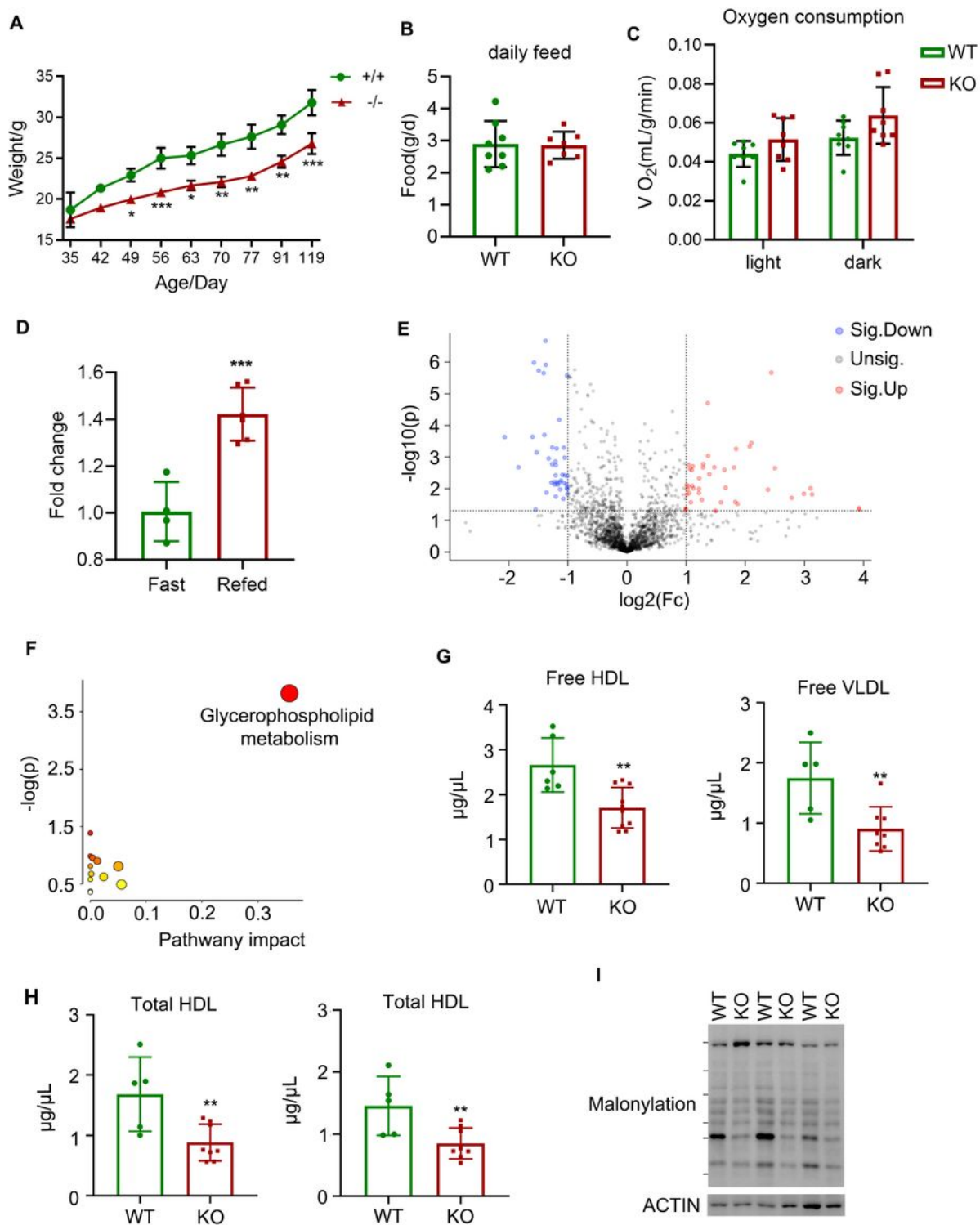


**Figure 3**

### Loss of TCAIM changes liver metabolism in mouse

**A.** The weight curve shows the bodyweight of TCAIM KO mice in comparison to its WT littermates. (n = 3, \*p < 0.05, \*\*p < 0.01, \*\*\*p < 0.001).

**B.** Daily food intake of TCAIM KO mice in comparison to WT littermates. (n = 8).

**C.** Oxygen consumption rates recorded by Comprehensive Lab Animal Monitoring System of TCAIM KO mice in comparison to WT littermates. (n = 8, light: n.s:  $p > 0.05$ , dark:  $*p < 0.05$ ).

**D.** The level of TCAIM mRNA in fast and refed mouse livers were tested by QPCR. Ten WT mice were fast for 20h and six of them were refed for 8h. ( $***p < 0.001$ )

**E.** Volcano plot showing the statistical significance (y axis) and fold change (x axis) for the difference between WT mice and TCAIM KO serum metabolite content. The red points represent up-regulated metabolites (adjusted  $P < 0.05$ ; fold change  $\geq 2$ ). The blue points represent down-regulated metabolites (adjusted p value  $< 0.05$ ; fold change  $\leq 2$ ).

**F.** Metabolomic Pathway Analysis was generated by MetaboAnalyst software package. All the matched pathways are displayed as circles. The color of each circle is based on p-values (darker colors indicate more significant changes of metabolites in the corresponding pathway), and the size of the circle corresponds to the pathway impact score. The most impacted pathways having high statistical significance scores are annotated.

**G-H.** Cholesterol Assay kit was used to test the level of Free (**G**) and total (**H**) cholesterol in WT or TCAIM KO mice serum (n > 3).

**I.** The protein malonylation level of WT and TCAIM KO mouse livers. The livers were lysed and then tested by immunoblotting (n > 3).

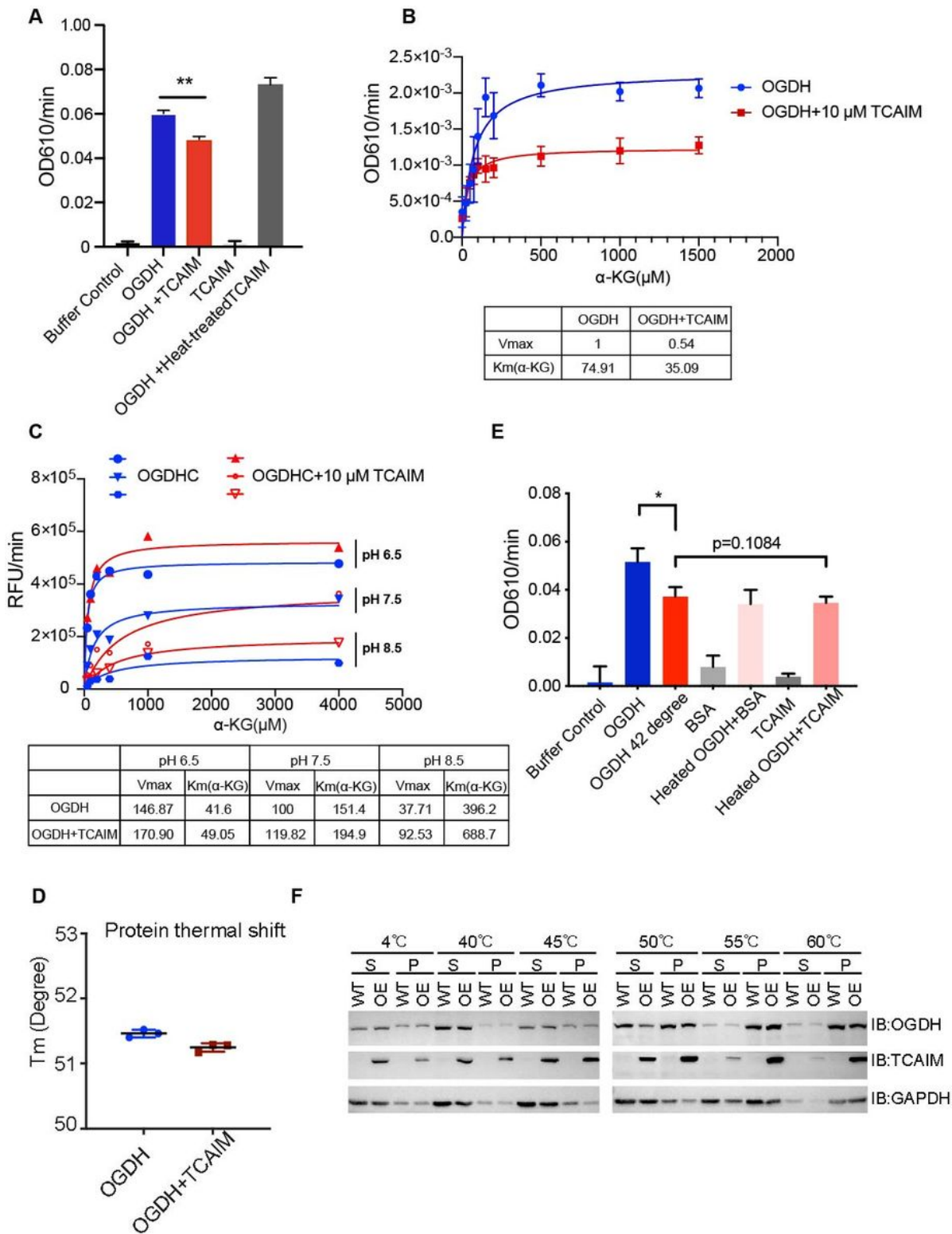


**Figure 4**

**TCAIM has no significant effect upon OGDH and OGDHC activities *in vitro***

**A.** OGDH activity was measured by DCPIP reduction rate at 610 nm. Purified TCAIM proteins (red), 95 °C heat-treated TCAIM (gray) were added to the OGDH activity assay system to evaluate their effects on

OGDH activity. Buffer and TCAIM proteins alone were used to replace OGDH for the same activity assay as a negative control (\*\*p < 0.01, n = 3).

**B.** The  $K_m$  and  $V_{max}$  of OGDH with (red) or without (blue) 10  $\mu\text{m}$  TCAIM was calculated by the  $V_0$  at different concentrations of  $\alpha$ -ketoglutarate using an *in vitro* assay.

**C.** The  $K_m$  and  $V_{max}$  of OGDHC with (red) or without (blue) 10  $\mu\text{m}$  TCAIM is calculated by the  $V_0$  at different concentrations of  $\alpha$ -ketoglutarate under different pH conditions using an *in vitro* assay.

**D.** OGDH (Blue), 42 °C -treated OGDH incubated with protein suspension buffer, TCAIM or BSA protein (red), as well as Buffer, BSA and TCAIM proteins alone (grey), as negative controls, measured for OGDH activities with DCPIP reduction rate (\*p < 0.05, n = 3).

**E.** SYPRO orange was mixed with purified OGDH protein or OGDH-TCAIM complex protein, and the fluorescence change of SYPRO orange at the temperature of 25-95°C was measured for  $T_m$ .

**F.** HEK 293T cells overexpressing TCAIM were lysed in MCLB. Supernatants were treated at different temperatures (4, 40, 45, 50, 55, 60 °C). After centrifugation, protein levels of OGDH, TCAIM and GAPDH in the supernatant and pellet were detected via western blot.

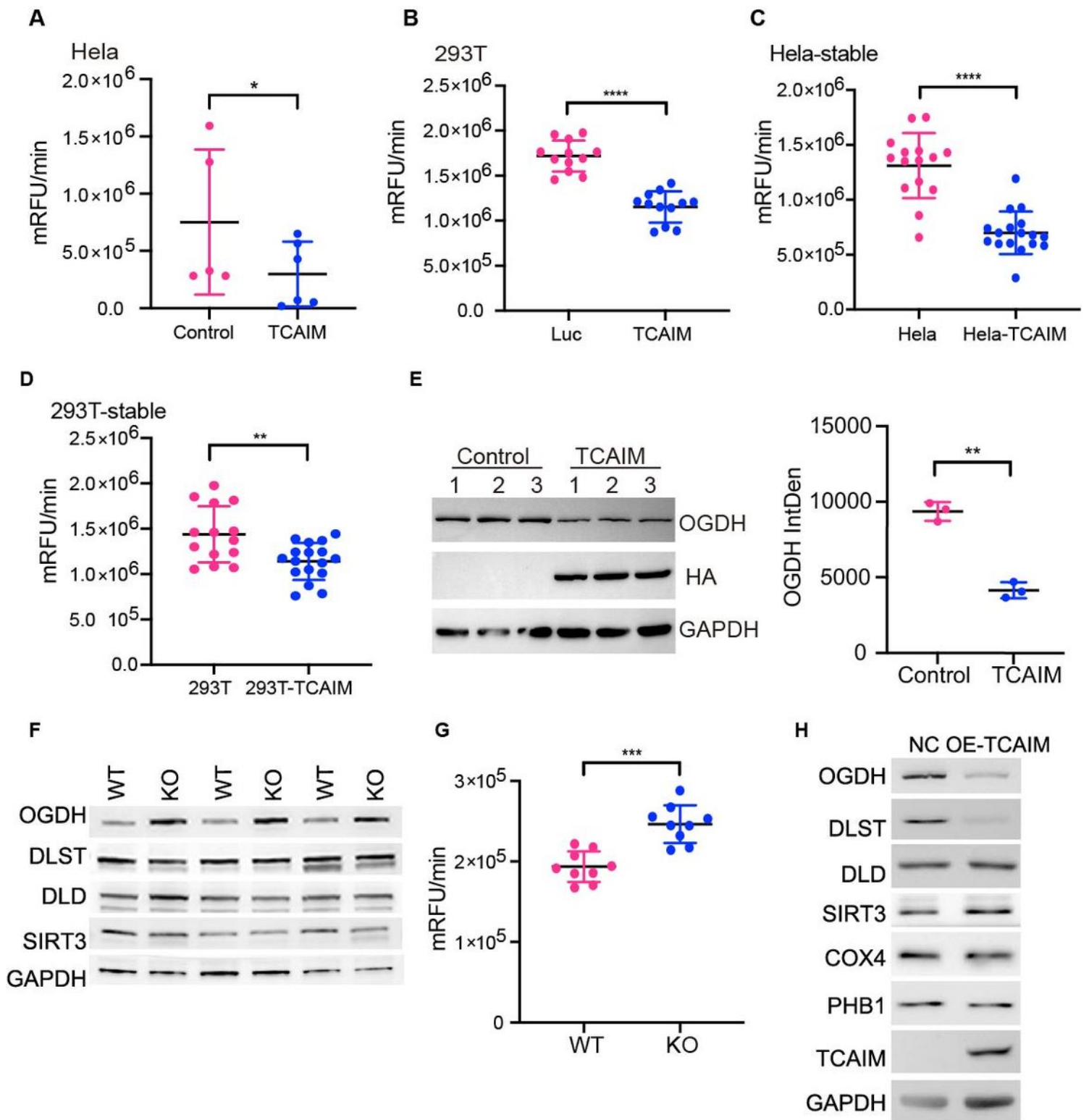


**Figure 5**

**TCAIM decreases OGDH protein level and OGDHC activities *in vivo***

**A.** OGDHC activities were calculated using OGDHC assay system from 20  $\mu$ g of purified cell lysates of TCAIM mRNA-transfected HeLa cells or that of Luciferase mRNA-transfected HeLa cells ( $p < 0.05$ ,  $n = 6$ ).

- B.** OGDHC activities were calculated using OGDHC assay system from 20 µg of purified cell lysates of TCAIM mRNA-transfected HEK293T cells or that of Luciferase mRNA-transfected HEK293T cells ( $p < 0.0001$ ,  $n = 12$ ).
- C.** OGDHC activities were calculated using OGDHC assay system from 20 µg of purified cell lysates of TCAIM stable overexpression HeLa cells or that of control HeLa cells ( $p < 0.0001$ ,  $n = 17$ ).
- D.** OGDHC activities were calculated using OGDHC assay system from 20 µg of purified cell lysates of TCAIM stable overexpression HEK293T cells or that of control HEK293T cells ( $p < 0.0001$ ,  $n = 17$ ).
- E.** The protein levels of OGDH, TCAIM-HA and GAPDH in HeLa cells that transiently overexpressed EGFP or TCAIM-HA mRNA were tested by immunoblotting (left). The band intensities of OGDH were quantified using ImageJ and normalized to the band intensities of GAPDH (right) ( $p < 0.01$ ,  $n = 3$ ).
- F.** The protein levels of OGDH, DLST, DLD, SIRT3 and GAPDH in the liver lysates of TCAIM KO mice and that of WT littermates were tested by immunoblotting.
- G.** Liver OGDHC activities were calculated using OGDHC assay system from 20 µg of purified TCAIM WT and KO liver lysates ( $p < 0.001$ ,  $n = 9$ ).
- H.** Protein levels of OGDH, TCAIM-HA and SIRT3, COX4, PHB1 in HeLa cells that transiently overexpressed EGFP or TCAIM-HA mRNA were tested by immunoblotting.

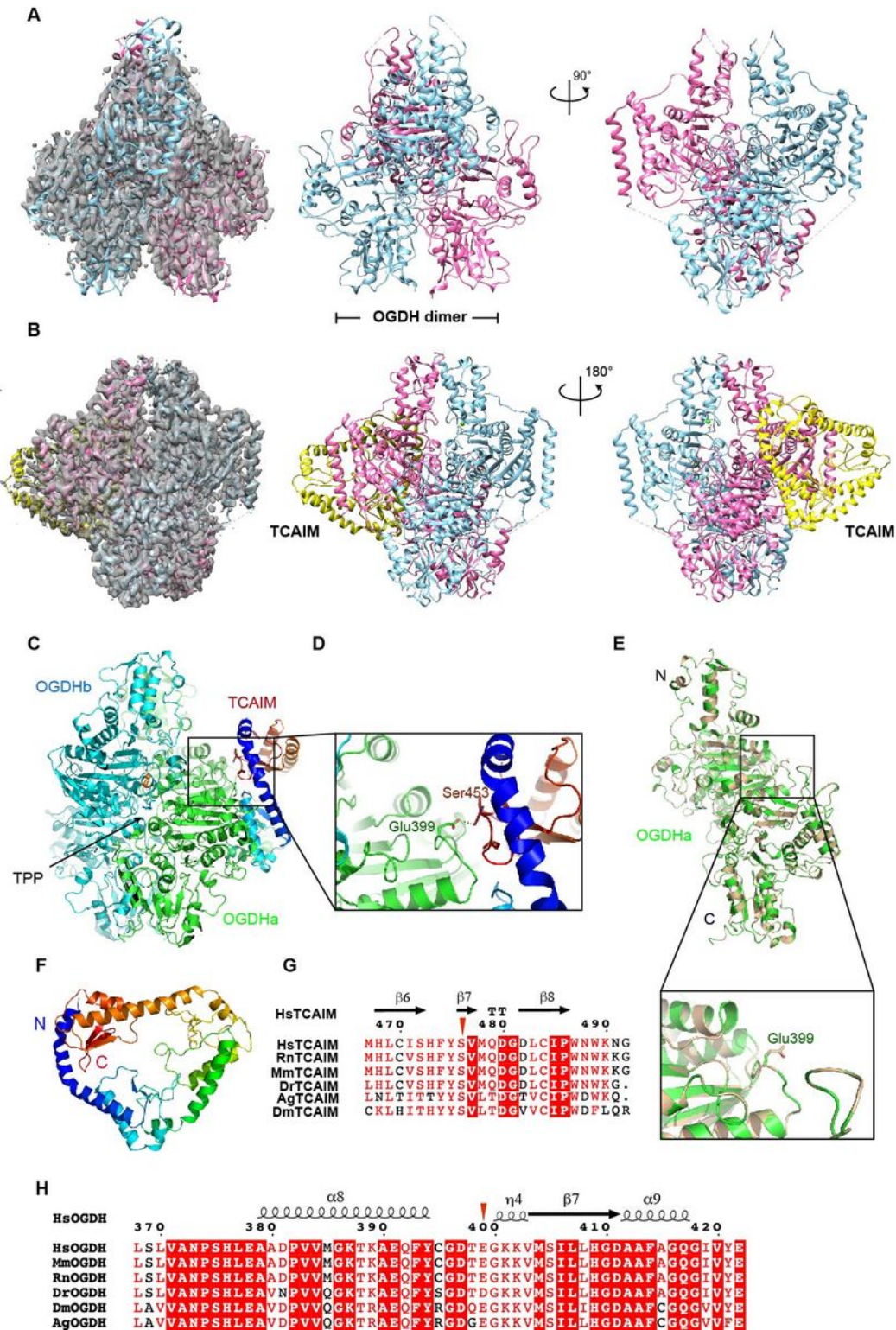


**Figure 6**

The Cryo-EM structure of TCAIM-OGDH shows that TCAIM binds to native OGDH

**A.** Cryo-EM structure of hsOGDH, density map (left panel), hsOGDH structure (middle and right panels), the structure shown as cartoon, chain-a colored in blue, and chain-b in violet.

- B.** Cryo-EM structure of hsOGDH-TCAIM complex, density map (left panel), hsOGDH-TCAIM complex structure (middle and right panels), the structure shown as cartoon, chain-a colored in blue, chain-b in violet and TCAIM in yellow.
- C.** Cartoon representation of OGDH-TCAIM complex, chain-a colored in green, chain-b in blue and TCAIM by rainbow. TPP shown as sticks.
- D.** Close-up view of interaction site of OGDH and TCAIM, residues involved in interactions shown as sticks.
- E.** Superimposition of OGDH apo and OGDH from the OGDH-TCAIM complex.
- F.** Cartoon representation of TCAIM, TCAIM colored in rainbow. The N terminal colored in blue; the C terminal colored in red.
- G.** Sequence alignment of TCAIM homologs from different species. Conserved amino acids marked with a red background, the TCAIM-OGDH interaction site marked by red inverted triangle. (Hs, *homo sapiens*; Mm, *Mus musculus*; Rn, *Rattus norvegicus*; Dr, *Danio rerio*; Dm, *Drosophila melanogaster*; Ag, *Anopheles gambiae*).
- H.** Homologous OGDH sequence alignment. Conserved amino acids shaded in red, the interaction site marked by red inverted triangle.

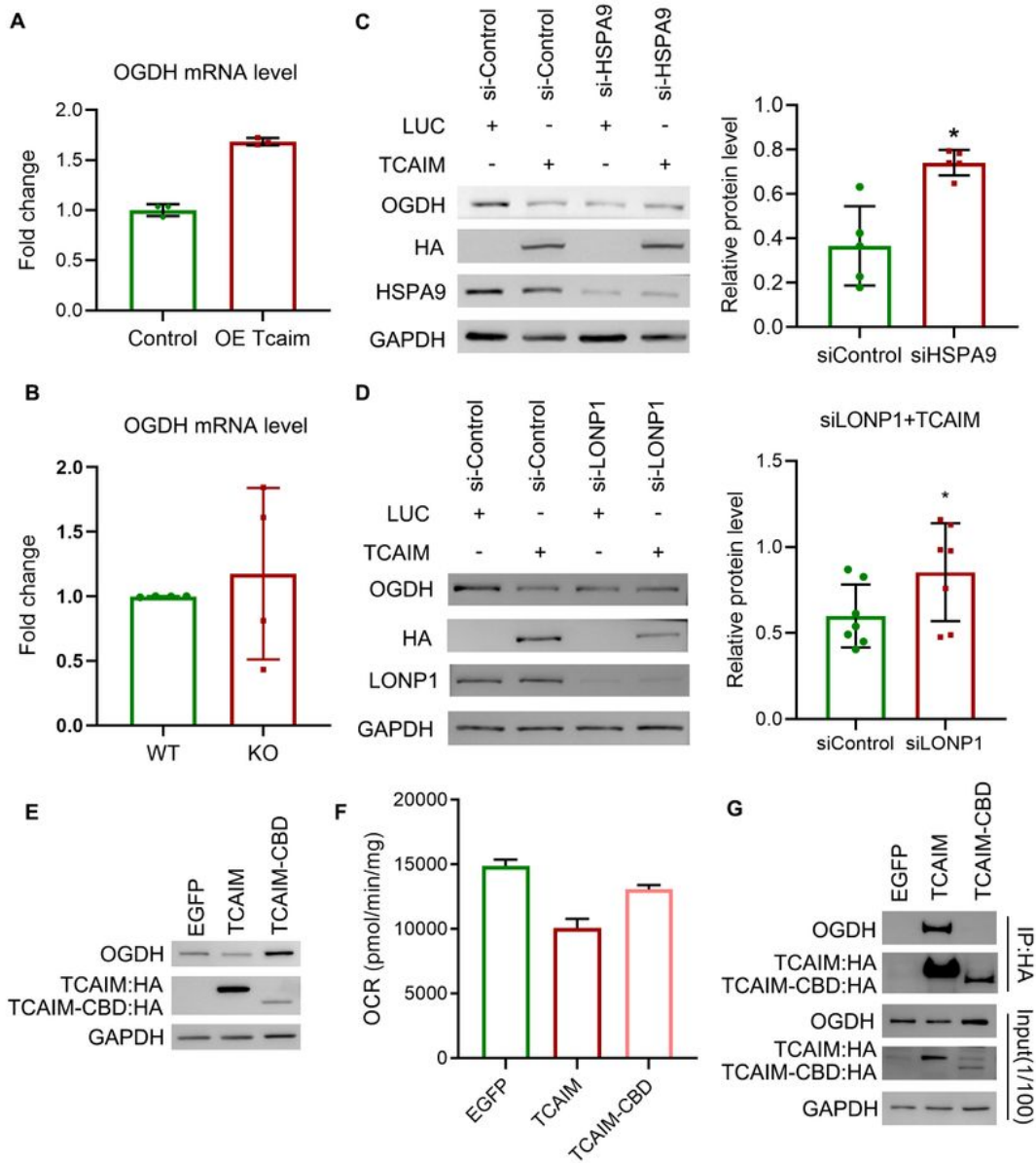


**Figure 7**

**TCAIM mediates the degradation of OGDH in a HSPA9- and LONP- dependent manner**

**A.** The mRNA level of OGDH in HeLa cells transiently overexpressing EGFP mRNA or TCAIM-HA mRNA, detected by relative quantitative QPCR.

- B.** The OGDH mRNA level in the livers of WT or TCAIM KO mice detected by relative quantitative QPCR.
- C.** The protein levels of OGDH, TCAIM-HA, HSPA9 and GAPDH in HeLa cells transiently knocked down for HSPA9 and transiently overexpressing EGFP mRNA or TCAIM-HA mRNA, measured by immunoblotting (left). The relative protein expression levels of OGDH were quantified from bands density using ImageJ and normalized to GAPDH (right) ( $p < 0.05$ ,  $n = 5$ ).
- D.** The proteins levels of OGDH, TCAIM-HA, LONP1 and GAPDH in HeLa cells transiently knocked down for LONP1 and transiently overexpressing EGFP mRNA or TCAIM-HA mRNA, measured by immunoblotting (left). The relative protein expression levels of OGDH were quantified from band densities using ImageJ and normalized to GAPDH (right) ( $p < 0.05$ ,  $n = 5$ ).
- E.** The protein levels of OGDH, TCAIM-HA or CBD-TCAIM-HA and GAPDH in HeLa cells transiently overexpressing EGFP, TCAIM-HA or CBD-TCAIM mRNA, measured by immunoblotting.
- F.** Co-immunoprecipitation using EGFP-HA, TCAIM-HA or TCAIM-CBD-HA as bait from the cell lysates of EGFP-HA, TCAIM-HA or TCAIM-CBD-HA mRNA-overexpressing HeLa cells and blotted with anti-OGDH, HA, or GAPDH antibodies.
- G.** The oxygen consumption rate (OCR) of HeLa cells transiently overexpressing EGFP, TCAIM or TCAIM-CBD mRNA, collected by Seahorse in serum-free basal DMEM containing 25 mM glucose and 4 mM glutamine.

## Supplementary Files

This is a list of supplementary files associated with this preprint. Click to download.

- [Table3CryoEMdatacollection.docx](#)
- [SupplTable1.xlsx](#)
- [Suppltable2.xlsx](#)
- [TCAIMsupplV1.docx](#)
- [D1300026625valreportfullannotateP1.pdf](#)
- [TCAIMsupplV1.docx](#)